

# A reduced model of neutral-plasma interactions in the edge and scrape-off-layer: verification comparisons with kinetic Monte Carlo simulations

D. A. Russell,<sup>1</sup> J. R. Myra<sup>1</sup> and D. P. Stotler<sup>2</sup>

<sup>1</sup> *Lodestar Research Corporation, Boulder, CO, USA*

<sup>2</sup> *Princeton Plasma Physics Laboratory, Princeton, NJ, USA*

August 2018 (revised Jan 2019)

submitted to Physics of Plasmas

---

DOE-ER/54392-91

LRC-18-176

---

**LODESTAR RESEARCH CORPORATION**

*2400 Central Avenue  
Boulder, Colorado 80301*

This report was prepared as an account of work sponsored by an agency of the United States Government. Neither the United States Government nor any agency thereof, nor any of their employees, makes any warranty, express or implied, or assumes any legal liability or responsibility for the accuracy, completeness, or usefulness of any information, apparatus, product, or process disclosed, or represents that its use would not infringe privately owned rights. Reference herein to any specific commercial product, process, or service by trade name, trademark, manufacturer, or otherwise does not necessarily constitute or imply its endorsement, recommendation, or favoring by the United States Government or any agency thereof. The views and opinions of authors expressed herein do not necessarily state or reflect those of the United States Government or any agency thereof.

**A reduced model of neutral-plasma interactions in the edge and scrape-off-layer:  
verification comparisons with kinetic Monte Carlo simulations**

D. A. Russell,<sup>1</sup> J. R. Myra<sup>1</sup> and D. P. Stotler<sup>2</sup>

<sup>1</sup>*Lodestar Research Corporation, 2400 Central Avenue, Boulder, Colorado 80301, USA*

<sup>2</sup>*Princeton Plasma Physics Laboratory, Princeton University, P. O. Box 451, Princeton,  
New Jersey 08543-0451, USA*

**Abstract**

The 2D scrape-off-layer turbulence code (SOLT) is extended to include neutral-plasma interactions. A Boltzmann equation is derived for the evolution of the bi-normally-averaged neutral distribution function,  $G(x, v_x, t)$ , in the radial dimension, and this evolution is included in the new code (nSOLT). Neutral-plasma interactions are mediated by charge-exchange (CX) and ionization rates based on poloidally-averaged plasma density and temperature. Good agreement is obtained between asymptotically stationary neutral density profiles from nSOLT simulations and those previously obtained from the Monte Carlo neutral transport code DEGAS 2, for time-averaged NSTX H-mode plasma profiles. The sensitivity of the nSOLT neutral profiles to atomic physics parameters, with and without CX physics, is included in the comparison. In addition, nSOLT simulations that *evolve* the plasma in 1D, using radial diffusion as a proxy for turbulent (blob) transport, illustrate the convergence to a *self-consistent* neutral-plasma equilibrium sustained by a neutral source at the far-SOL boundary and plasma heating in the core; equilibria consistent with typical NSTX Ohmic L-mode plasmas are described.

## I. Introduction

The importance of accounting for neutral interactions in modeling plasma turbulence and transport in the tokamak edge and scrape-off-layer (SOL) is irrefutable. The tokamak plasma is maintained against losses by an influx of neutral atoms in the form of beams, gas puffs, and/or recycled plasma ions from material surfaces. Neutral ionization by electron collisions is concentrated in the edge and near-SOL where the electron temperature exceeds the ionization energy, and ionization here cools the plasma, while charge-exchange collisions produce a population of heated neutrals that can escape through the relatively cool SOL and impact the wall, causing impurity sputtering, enhanced recycling and damage to plasma-facing components. Momentum exchange with neutrals results in forces that can drag the plasma flows. The ionization particle source and energy sink can also modify plasma and hence flow profiles. Both effects can impact the formation of transport barriers and the moderation of instabilities by sheared flows. Historically, these effects have been included in large-scale plasma transport codes by coupling them to kinetic Monte Carlo neutral transport codes. But *reduced* modeling of *self-consistent* interactions between neutrals and *turbulent* plasma fluctuations is in its early stages of development at this writing.

A brief roundup of currently active modeling capabilities affords perspective on the reduced model presented here. The most realistic models of plasma transport in the edge and SOL are provided by gyro-kinetic particle-in-cell (PIC) codes. For example, XGC1 [1] evolves turbulent plasma fluctuations in three spatial dimensions (3D) in diverted magnetic field geometry and includes self-consistent neutral-plasma interactions via a built-in Monte Carlo (MC) neutral transport routine. [2] In order to reach statistically steady states that emerge on the longest “transport” time scales the extreme realism afforded by this coupled system comes at a relatively high cost, making it desirable to conduct studies of neutral-plasma equilibria, for a range of input parameters and on realistic wall-clock time scales, using reduced-model simulations.

Fluid models of plasma turbulence offer a significant reduction in computational cost compared to PIC models. For describing edge and SOL turbulence, these models are dominated by the drift-reduced Braginskii equations.[3] Simulation models that solve these (or closely related) fluid equations include: the BOUT++ package [4]; the GBS (“Global Braginskii Solver”) code [5]; the GDB (“Global Drift-Ballooning”) code [6], the HERMES code [7] (built on the BOUT++ package), the HESEL (“Hot Edge-Sol-Electrostatic”) code [8], the SOLT (“Scrape-Off-Layer Turbulence”) code [9] and the TOKAM3X code.[10] The Braginskii model [3] describes the evolution of fluctuations on spatial scales perpendicular to the magnetic field limited by the ion gyro-radius and time scales greater than the ion gyro-period, and while the equations solved in these codes differ in important details (electromagnetic capability, dimensionality, magnetic field realism and the Boussinesq approximation [11]), all resolve “blob” fluctuations born of the interchange instability in the edge region and the associated turbulent transport. (See references [12, 13] for a review of transport by blob-filaments.)

Although the more physically realistic and expensive of these models may be reduced further to run faster (e.g., BOUT++ and GBS *can* be run in 2D mode), that is counter to their purpose: to provide a global picture of fully 3D turbulent fluctuations for realistic tokamak magnetic field geometry. The reduced models serve both to resolve details of the turbulence in spatially localized critical sub-domains of the big picture, e.g., the outboard midplane (OM) sub-domain of the edge and SOL, and to achieve self-consistent equilibria between the radial plasma profiles (mean fields) and the fluctuations, and to do so economically. In this sense, HESEL and SOLT are the most reduced of the fluid turbulence models listed above simply because their simulation domain is a plane perpendicular to the B-field in the OM region and because of other physics simplifications that distinguish them in detail.

If instead a 3D fluid model is reduced to 2D by replacing the fluctuations with their toroidal averages (i.e., assuming toroidal axisymmetry), equilibria are more economically attained. If, in addition, the particle and energy transport perpendicular to the magnetic flux surfaces is modeled by “anomalous” diffusion coefficients (intended to account for turbulent diffusion and convection), then the result is a “transport” model. Transport models can describe equilibrium plasma profiles on the global scale for realistic tokamak B-field geometry. The effect that neutrals have on the equilibria is typically studied by coupling the plasma-transport code to either a fluid neutral model, such as UEDGE,[14] or to a kinetic Monte Carlo neutral-transport code, for example in the EDGE2D-EIRENE [15] and UEDGE-DEGAS 2 [16] couplings and in the B2.5-EIRENE [17] coupling in the SOLPS-ITER [18] system. These neutral-plasma transport systems are relatively expensive to run, and the MC codes are a source of some noise. (Both B2.5 and UEDGE include fluid-neutral modules that can serve as simpler, faster and quieter alternatives to the MC routines.) Furthermore, the anomalous diffusion coefficients must be chosen *ab initio* and are not determined self-consistently in the course of the simulation, making them arguably *ad hoc*, or at best empirical; for studying self-consistent neutral-*turbulent*-plasma interactions, these codes are inappropriate.

The high cost of iterating a *turbulent* plasma transport code coupled to a MC neutral-transport code, long enough to reach equilibrium, compels the development of reduced neutral-plasma interaction models. Indeed, to our knowledge, none of the Braginskii fluid models have been coupled to a MC neutral transport model, although this was reported as a work-in-progress in the case of the TOKAM3X code (coupled to EIRENE) in reference [10]. Instead, the fluid models may be extended to include either a kinetic Boltzmann description or a fluid description of neutral transport, with the plasma interaction provided by formulaic collision rates. The fluid-neutral description is appropriate in the short neutral mean-free-path (MFP) regime, and the kinetic-neutral description in the long MFP regime. MC PIC models include both regimes.

The development of reduced neutral-*turbulent*-plasma interaction models, either fluid- or kinetic-neutral, to study edge and SOL turbulence represents a rapidly changing field populated by only a few examples at this writing. The fluid-neutral models include those of Bisai and Kaw [19] (BK) and a recent extension of the HESSEL model. [20] The GBS model[5] is the only

reduced fluid-plasma coupling to kinetic (Boltzmann) neutrals, besides the one proposed here, of which we are aware.

The 2D BK fluid model describes the evolution of the electron, ion ( $H^+$  and  $H_2^+$ ) and neutral densities, the electron temperature and the electrostatic potential using fluid moment equations. Neutral transport is diffusive, and the diffusion coefficient depends on ionization, charge-exchange and molecular dissociation collision rates. The model has been applied to study neutral effects on plasma density, temperature and electrostatic potential profiles in the SOL. (Ions and neutrals were taken to be cold in [19], while a population of hot neutrals was modeled in [21].) The nHESSEL model is similar to the BK model in that it couples reduced fluid-plasma evolution equations for density, potential, and electron and ion pressures to the diffusive evolution of several species of energetically distinguished fluid-neutrals. It has been applied recently to study blob-neutral interactions in the presence of molecular dissociation. [22] (SOLT can be extended similarly to include a 2D neutral fluid model, but that is not described in this paper.)

The GBS code has been extended recently to include self-consistent kinetic neutral-plasma interactions. [5] The neutrals evolve according to a 3D kinetic equation for the distribution function coupled to the plasma through the use of Krook operators based on collision rates for ionization, charge-exchange and recombination, and the plasma evolves according to the drift-reduced Braginskii equations expanded by the corresponding neutral collision terms. This model can describe both long and short neutral MFP regimes. Simplifying assumptions related to the anisotropy of blob filaments and to the separation of characteristic times for turbulent fluctuations and for neutral flights are exploited to reduce the 3D model to a set of coupled problems on 2D poloidal sections. The nSOLT model described here is a further reduction that focuses on 2D plasma evolution in the outboard midplane region coupled to long-MFP neutral evolution described by a 1D Boltzmann equation.

The primary shortcoming of the fluid-neutral model is that it does not describe the long MFP neutrals produced by charge-exchange in the edge region. These effectively heated neutrals penetrate into the edge pedestal where they are further heated and then can cross the SOL to impact the wall where they contribute to recycling and erosion. Although this population may be a relatively tenuous tail on the neutral distribution function, the corresponding energy flux to the wall (a third-order velocity moment) may contribute to the heat load limits on the first wall [23] and cause long-term damage and erosion of material surfaces. The neutral particle flux contributes as well to recycling. The fluxes can only be measured with confidence in a kinetic-neutrals simulation like the extended GBS model and the nSOLT model introduced here.

The nSOLT model is a 2D fluid-plasma, 1D kinetic-neutral (Boltzmann) model applicable in cases where the neutrals have ionization MFPs that are long compared to plasma turbulence (blob) structure sizes. This is arguably the case for atomic neutrals born from molecular dissociation ( $\sim 3$  eV Franck-Condon atoms) near material boundaries in the far-SOL [24] and, all the more so, for neutrals effectively heated by charge exchange with hot ions ( $\sim 100$  eV) in the edge region. In the 1D model, turbulence structures interact with neutrals through

poloidal ( $y$ ) averages, i.e., the neutrals “average over” the turbulence by virtue of their relatively long MFPs. For example, the neutral shadow [25] cast by a plasma blob may show up as a negative fluctuation in the radial neutral density profile, provided the blob shows up in the SOL plasma profile. This admittedly limited description may suffice for modeling the self-consistent evolution of neutral and plasma profiles. Where this is the case, nSOLT will find equilibria that may prove predictive of conditions in the tokamak SOL, and do so quite economically.

The remaining sections of this paper are organized as follows. Section II introduces the nSOLT model equations, with details given in an appendix. Section III presents results from a verification exercise: taking fixed plasma profiles from NSTX H-mode discharges, stationary atomic (D) density profiles obtained from nSOLT and from DEGAS 2 MC [26] simulations are compared. In Sec. IV, results from 1D nSOLT simulations of *time-dependent*, self-consistent neutral-plasma evolution are described. In these simulations linear radial diffusion serves as a proxy for turbulent transport. Self-consistent equilibria are obtained for neutral fueling at the far-SOL boundary and plasma heating in the core region. A summary and concluding remarks are given in Sec. V.

## II. The nSOLT model

### 1. Neutral-plasma evolution equations

The evolution of the neutral species is described by the following equations

$$\partial_t G + v_x \partial_x G = h_{cx} n_0 F - h_{cx} \bar{n}_i G - h_{iz} \bar{n}_e G \quad (1a)$$

$$\partial_t v_{0y} + v_{0x} \partial_x v_{0y} = h_{cx} \bar{n}_i (\bar{v}_{Ey} + \bar{v}_{diy} - v_{0y}) \quad (1b)$$

where  $G = G(t, x, v_x)$  is the 1D neutral species distribution function, and  $F = F(t, x, v_x)$  is a 1D Maxwellian distribution function based on the poloidally averaged ion density and temperature,

$$F = \bar{n}_i \exp\left[-v_x^2 / (2\bar{T}_i)\right] / (2\pi\bar{T}_i)^{1/2}.$$

Here  $x$  is the radial dimension and the over-bar denotes a poloidal ( $y$ ) average,  $n_i$  and  $n_e$  are the ion and electron number densities, and  $v_{Ey}$  and  $v_{diy}$  are the  $y$ -components of the  $E \times B$  and ion diamagnetic drift velocities, respectively. All plasma quantities ( $n_i$ ,  $n_e$ ,  $v_{Ey}$ ,  $v_{diy}$ ) are represented by their poloidal averages in Eqs. (1), corresponding to the long-MFP neutral limit where the neutrals average over the turbulence. The neutral density and radial neutral fluid velocity,  $n_0$  and  $v_{0x}$ , are obtained from the moments of  $G$ ,

$$n_0 = \int dv_x G(x, v_x, t), \quad v_{0x} = \int dv_x v_x G(x, v_x, t) / n_0,$$

and  $v_{0y}$  is the poloidal neutral fluid velocity. Details of the reduction of the 3D Boltzmann equation to 1D, Eq. (1a), and the derivation of Eq. (1b) are given in the appendix.

The charge exchange (CX) and ionization (IZ) rates per particle ( $h_{cx}$  and  $h_{iz}$ ) appear as multipliers in Eqs. (1) because the collision rates,  $\sigma(\mathbf{v}, \mathbf{v}')|\mathbf{v} - \mathbf{v}'|$  have been approximated by their averages over assumed Maxwellian distributions of ion and electron velocities in the Boltzmann collision integral:  $h_{cx}(T_i) = \langle \sigma_{cx} |\mathbf{v}_i| \rangle$  and  $h_{iz}(T_e) = \langle \sigma_{iz} |\mathbf{v}_e| \rangle$ . Note that we ignore radiative recombination altogether in the model because the rate per particle for that process ( $h_{rec}$ ) is much less than either  $h_{cx}$  or  $h_{iz}$  for the plasma temperatures considered here, viz. midplane modeling of the edge and main SOL. Recombination would be important if the model were adapted for application to the divertor region in detached conditions. See the appendix (A4) for details.

The plasma evolution is described by the SOLT model equations, [9] expanded to include neutral interactions by the addition of the terms, derived in the appendix A(1-2), proportional to  $h_{cx}$  and  $h_{iz}$  in Eqs. 2(a-c) and the term involving  $f$  in Eq. 2(d) below:

$$d_t n_e = \nabla \cdot (D_n \nabla n_e) + S_n + h_{iz} n_0 n_e - \nabla_{//} \Gamma_{//}, \quad (2a)$$

$$d_t T_e = \nabla \cdot (D_{Pe} n_e \nabla T_e) / n_e - T_e \nabla \cdot (D_n \nabla n_e) / n_e + (S_{Pe} - T_e S_n) / n_e + \\ - h_{iz} n_0 \left( \frac{2}{3} E_{iz} + T_e \right) - \frac{2}{3n_e} \nabla_{//} q_{e//} + \frac{T_e}{n_e} \nabla_{//} \Gamma_{//}, \quad (2b)$$

$$d_t T_i = \nabla \cdot (D_{Pi} n_i \nabla T_i) / n_i - T_i \nabla \cdot (D_n \nabla n_i) / n_i + (S_{Pi} - T_i S_n) / n_i + \\ + (h_{iz} + h_{cx}) n_0 \left( \frac{2}{3} E_0 - T_i \right) - \frac{2}{3n_i} \nabla_{//} q_{i//} + \frac{T_i}{n_i} \nabla_{//} \Gamma_{//}, \quad (2c)$$

$$d_t \rho = \nabla^2 (D_\rho \rho) - 2\mathbf{b} \times \kappa \cdot \nabla (P_e + P_i) - (\partial_x f_y - \partial_y f_x) - \nabla_{//} j_{//} + \\ + \frac{1}{2} \left[ n_e v_{di} \cdot \nabla \nabla^2 \phi \right] - \frac{1}{2} \left[ \mathbf{v}_E \cdot \nabla (\nabla^2 P_i) - \nabla^2 (\mathbf{v}_E \cdot \nabla P_i) \right] - \frac{1}{2} \mathbf{b} \times \nabla n_e \cdot \nabla v_E^2, \quad (2d)$$

with the generalized vorticity

$$\rho = -\nabla \cdot (\mathbf{n} \nabla \phi + \nabla P_i). \quad (2e)$$

Here  $d_t = \partial_t + \mathbf{v}_E \cdot \nabla$  is the total time derivative including convection by the  $\mathbf{E} \times \mathbf{B}$  velocity,  $\mathbf{v}_E = \mathbf{b} \times \nabla \phi$ , in a constant, uniform magnetic field  $\mathbf{B} = b\mathbf{B}$  directed out of the (x,y) plane that is the domain of the model. The ion diamagnetic drift velocity is given by  $\mathbf{v}_{di} = \mathbf{b} \times \nabla P_i / n_i$ . The electron and ion pressures are given by  $P_e = n_e T_e$  and  $P_i = n_i T_i$ , respectively. Although we have distinguished between electron and ion densities in Eqs. (1) and (2), the model assumes quasi-neutrality ( $n_e = Zn_i$ ), and we treat only deuterium plasmas here ( $Z = 1$ ). The equations are given in dimensionless form in Bohm units of time ( $\Omega_{ci}^{-1}$ ), length ( $\rho_s = c_s / \Omega_{ci}$ ) and electrostatic potential ( $T_{ref}/e$ ), where the ion cyclotron frequency is  $\Omega_{ci} = ZeB/m_i c$ , and the ion acoustic speed

is  $c_s = (ZT_e/m_i)^{1/2}$ . Temperature and density are normalized by reference values:  $(n_{\text{ref}}, T_{\text{ref}}) = (10^{13} \text{cm}^{-3}, 100 \text{eV})$  in this paper.

The parallel current density ( $j_{\parallel}$ ), particle flux ( $\Gamma_{\parallel}$ ) and heat fluxes ( $q_{e\parallel}$  and  $q_{i\parallel}$ ) are based on models of 1) electrostatic drift wave physics in the closed-field -line or “core” region and of 2) divertor sheath physics (via “closure” relations) in the open field line region, i.e., in the SOL. These are dynamical quantities that evolve with the turbulent plasma fields. We refer the reader to our published work, [27] for a complete description of these terms.  $S_n$ ,  $S_{Pe}$  and  $S_{Pi}$  are specified sources of plasma density, electron pressure and ion pressure, respectively.

The factor  $2/3$ , multiplying the ionization cost ( $E_{iz}$ ) and the neutral energy ( $E_0$ ) in Eqs. (2a) and (2b), results from the assumption that the neutrals are isotropically distributed in velocity space; see the appendix (A2).

The vector

$$\mathbf{f} \equiv h_{\text{CX}} n_0 n_i (\mathbf{v}_0 - \mathbf{v}_E - \mathbf{v}_{\text{di}}) + h_{\text{IZ}} n_0 n_e \mathbf{v}_0 \quad (2f)$$

in the vorticity equation (2d) describes the neutral drag of the plasma flows by CX and IZ “friction” forces. The expression given for the effect of this force density on the vorticity evolution, viz.,  $\mathbf{b} \cdot \nabla \times \mathbf{f} = \partial_x f_y - \partial_y f_x$ , is of the same form as that more familiar expression for the effect of the polarization force, due to B-field curvature and grad-B drifts, given by  $2\mathbf{b} \times \boldsymbol{\kappa} \cdot \nabla (P_e + P_i)$  in Eq. (2d). (The dimensionless curvature vector  $\boldsymbol{\kappa} = \mathbf{b} \cdot \nabla \mathbf{b}$ .) The neutral force is simply added to a general expression for the effect of polarizing forces on the evolution of vorticity. [12] The neutral density  $n_0$  and velocity  $\mathbf{v}_0$  are functions only of radius ( $x$ ) and time ( $t$ ), while the plasma fields ( $n_i$ ,  $n_e$ ,  $\mathbf{v}_E$  and  $\mathbf{v}_{\text{di}}$ ) are functions of  $x$ , bi-directional (approximately poloidal) dimension ( $y$ ) and time.

## 2. Boundary conditions

All plasma fields ( $n$ ,  $T_e$ ,  $T_i$ ,  $\phi$ ) are periodic in  $y$ . The fluctuations in these fields (e.g.,  $\delta n = n - \bar{n}$ , where the over-bar indicates the poloidal average or “mean” value) vanish at both  $x$ -boundaries of the domain  $0 \leq x \leq L_x$ . The mean values of the density and temperatures are held to constant “floor” values at the far-SOL boundary, and their radial gradients are held to zero at the core-side boundary so that there is no diffusive flux of those quantities at that boundary. Either the potential ( $\bar{\phi}$ ) or the radial electric field ( $-\partial_x \bar{\phi} = -\bar{v}_{EY}$ ) may be specified at the  $x$ -boundaries, and these boundary conditions are used to solve Eq. (2e) for the potential.

At the far-SOL boundary ( $x = L_x$ ), or “wall,” the boundary condition on  $G$  is given by Eqs. (3) and (4) below and describes neutral injection by a stationary source, or neutral gas “puff,” and time-dependent recycling of the ions. In Sec. III, the in-coming neutrals are taken to be Franck-Condon (FC) deuterium atoms (D) born from dissociation of the molecular species

(D<sub>2</sub>). We assume a Maxwellian distribution of velocities at a characteristic temperature ( $T_{FC}$ ) centered on the average velocity ( $v_{D_2}$ ) of the molecules entering from the wall:

$$G(x=L_x, v < 0) = N \exp[-(v - v_{D_2})^2 / 2T_{FC}] / (2\pi T_{FC})^{1/2}. \quad (3)$$

The density  $N$  is the sum of the puff ( $N_0$ ) and recycled neutrals and ions impacting the wall,

$$N = N_0 + (R_0 F_N + R_i \langle F_i \rangle_y) / v_{FC}^{(-)}, \quad (4)$$

where  $R_0$  and  $R_i$  are recycling coefficients,  $v_{FC}^{(-)} = - \int_{-\infty}^0 dv v \cdot f_{FC}(v)$ , and the out-going radial particle fluxes are given by

$$F_N = \int_0^{\infty} dv v G(v, x_{SOL}) \quad (5)$$

and

$$F_i = n_i \left[ \left( \frac{T_i}{2\pi} \right)^{1/2} \exp\left(-v_{Ex}^2 / 2T_i\right) + \frac{1}{2} v_{Ex} \operatorname{erfc}\left(-v_{Ex} / (2T_i)^{1/2}\right) \right], \quad (6)$$

where we have assumed a Maxwellian ion velocity distribution function centered at the radial  $E \times B$  velocity ( $v_{Ex}$ ) in Eq. (6), and  $\operatorname{erfc}$  denotes the complemented error function. As  $v_{Ex} / T_i \rightarrow \infty$  in Eq. (6), the ion flux,  $F_i$ , approaches  $n_i v_{Ex}$ , the ‘‘blob limit.’’ In the opposite extreme, i.e.,  $v_{Ex} / T_i \rightarrow 0$ ,  $F_i$  approaches the thermal limit,  $n_i (T_i / 2\pi)^{1/2}$ . The plasma fields in Eq. (6) are evaluated at the wall, and only the poloidal average of the ion flux contributes to recycling, as indicated in Eq. (4). In equation (3), we take  $v_{D_2} = -0.8$  km/sec, corresponding to room temperature (300° K) D<sub>2</sub> molecules that detach from the wall, and we take  $T_{FC} = 3$  eV, unless noted otherwise.

Neutrals free-stream out of the simulation domain at both boundaries; exiting neutrals at the core-side boundary,  $G(x=0, v < 0)$ , and at the first wall boundary,  $G(x=L_x, v > 0)$ , are evolved by convection alone. No neutrals enter from the core:  $G(x=0, v > 0) = 0$ .  $G$  is held to zero at the boundary of the velocity domain which extends to  $(\pm) 4c_s$  (280 km/sec) and adequately contains the observed support of  $G$  in the simulations. The boundary values of the poloidal neutral fluid velocity  $v_{0y}$  respond to the CX friction force according to Eq. (1b).

### 3. Numerical method for neutral evolution

Compared to some of the algorithms already in SOLT to evolve the plasma, those added to advance G are relatively trivial in structure and computational expense. Evolution is in three steps: free-streaming by upwind linear interpolation, CX update by a 2<sup>nd</sup> order Runge-Kutta method and an explicit exponential update for ionization. (Plasma fields are taken as fixed over a single time step,  $\Delta t$ .) The free-streaming update is constrained by  $\max(|v_x|) \Delta t / \Delta x < 1$ , where here  $v_x$  is the independent velocity variable of the neutral grid  $(x, v_x)$ . With  $\max(|v_x|) \sim c_s$  and  $\Delta x \sim \rho_s$ , this constraint amounts to  $\Delta t < \Omega_i^{-1}$  which imposes no greater computational burden than that imposed by resolving the turbulent fluctuations, where  $\Delta t \sim 10^{-2} \Omega_i^{-1}$  is typical in practice.

### III. nSOLT and DEGAS 2 comparisons

As a first verification exercise for nSOLT, we compare neutral deuterium (D) radial density profiles obtained from nSOLT simulations with those obtained from DEGAS 2 simulations using time-averaged plasma profiles measured on NSTX during H-mode discharges. [28] The plasma fields ( $n_e$ ,  $n_i$ ,  $T_e$ ,  $T_i$ ) do not evolve, while the neutrals evolve into stationary profiles. There is no  $y$ -dependence and, therefore, no turbulence (blobs) in the nSOLT simulations described here. The DEGAS 2 simulations are fully 3D but do not model plasma turbulence either. This is simply a test of the 1D neutral model in nSOLT and the stationary neutral density profiles that it predicts in equilibrium with given stationary plasma profiles. The electrostatic potential and plasma flows were not measured, so we do not evolve the neutral poloidal velocity in this exercise. *We suppress the over-bars, denoting  $y$ -averages, in this and the following section, and since the neutral atomic species is deuterium (D), we make the replacements  $n_0 \rightarrow n_D$  and  $E_0 \rightarrow E_D$ .*

The plasma profiles input to the DEGAS 2 simulations were measured by Thomson scattering (TS) and charge-exchange recombination spectroscopy (CHERS) on H-mode discharges at NSTX during the 2010 campaign. We make comparisons with two of the shots, 142214 and 139412, used in the DEGAS 2 simulations described in reference [28]. The plasma profiles for the shots are available from the archived data. [29] The  $n_e$  and  $T_e$  profiles for the nSOLT simulations are interpolations of the TS data, taken in the outboard midplane, and are shown in Fig. (1).

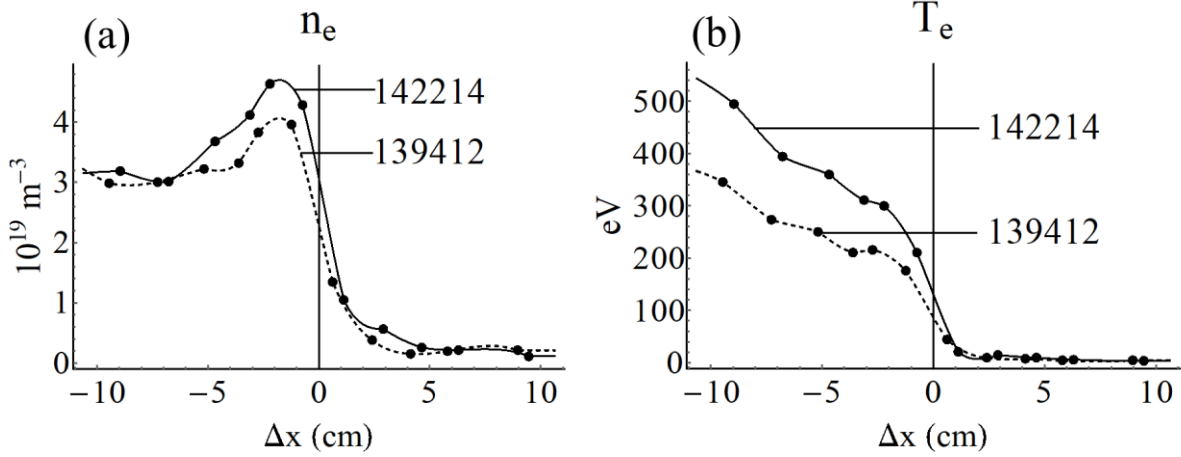


Fig. 1. Electron density (a) and temperature (b) profiles from Thomson scattering data (dots) interpolated (dashed and solid curves) onto the nSOLT radial grid and taken as input to the simulations.  $\Delta x$  is the displacement from the separatrix measured at the outboard midplane. The shot numbers appear as insets labeling the curves. [Associated dataset available at <https://doi.org/10.5281/zenodo.1342773>]

For these comparisons we take the electron density in nSOLT to be enhanced over the deuterium ion species ( $n_i$ ) by the presence of a minority population of carbon ions ( $C^{+6}$ ), consistent with the DEGAS 2 simulations. Thus in Eq. (1a) we take  $n_i = r n_e$ , where  $r = 0.8$  and  $0.86$  for shots 142214 and 139412 respectively. Because the CHERS diagnostic showed no significant difference between the electron and ion temperatures, they were taken to be equal in the DEGAS 2 and nSOLT simulations:  $T_i = T_e$ .

The CX and IZ rates used in the nSOLT simulations are [2]

$$h_{\text{cx}}(T_i) = 1.1 \times 10^{-14} T_i(x,t)^{0.3} M_i^{-1/2} \text{ m}^3/\text{sec} \text{ and} \quad (7)$$

$$h_{\text{iz}}(T_e) = 8 \times 10^{-15} T_e(x,t)^{1/2} \exp[-13.56/T_e(x,t)] / (1 + 0.01 T_e(x,t)) \text{ m}^3/\text{sec}, \quad (8)$$

respectively, with  $T_e$  and  $T_i$  expressed in eV and  $M_i$  in AMU ( $M_i = 2$  for D). These formulaic rates, equations (7) and (8), are fits to tabulated values of the collision rates that are used in the DEGAS 2 simulations. (See [28] and references therein.) The tabulated ionization rate is obtained from a collisional radiative model and is a function of the local electron temperature *and density*, while the tabulated CX rate is a function of the local ion temperature *and neutral D energy*  $E_D$ . Comparing the tabulated and formulaic rates we found that the ionization rate fit is within 20% of the tabulated value if  $10^{17} \text{ m}^{-3} < n_e < 10^{19} \text{ m}^{-3}$  and  $5 \text{ eV} < T_e < 5 \text{ keV}$ , and the CX rate fit is within 20% of the tabulated value if  $1 \text{ eV} < E_D < 20 \text{ eV}$  and  $T_i > 10 \text{ eV}$ . Of these bounds, the upper bound on the neutral energy (20 eV) is particularly exceeded for CX-heated D in the nSOLT simulations. (The D energy flux to the wall is maximized at  $E_D \cong 500 \text{ eV}$  in the

DEGAS 2 comparison runs.) So our neglect of  $E_D$  in Eq. (7) may not be justified and remains to be explored. Nevertheless, we shall see that good agreement with DEGAS 2 results is obtained.

The boundary condition for G at the wall corresponds to sustained neutral fueling with no recycling;  $N_0 > 0$ ,  $R_0 = 0$  and  $R_i = 0$  in Eq. (4). The absence of wall recycling is artificial; for this verification exercise we chose  $N_0$  so that the atomic deuterium density matched that observed in the DEGAS 2 simulations at a point in the SOL corresponding to the boundary of the nSOLT simulations, and we evolved Eq. (1a) until a stationary state was reached. The resulting neutral density profiles are compared in Fig. (2).

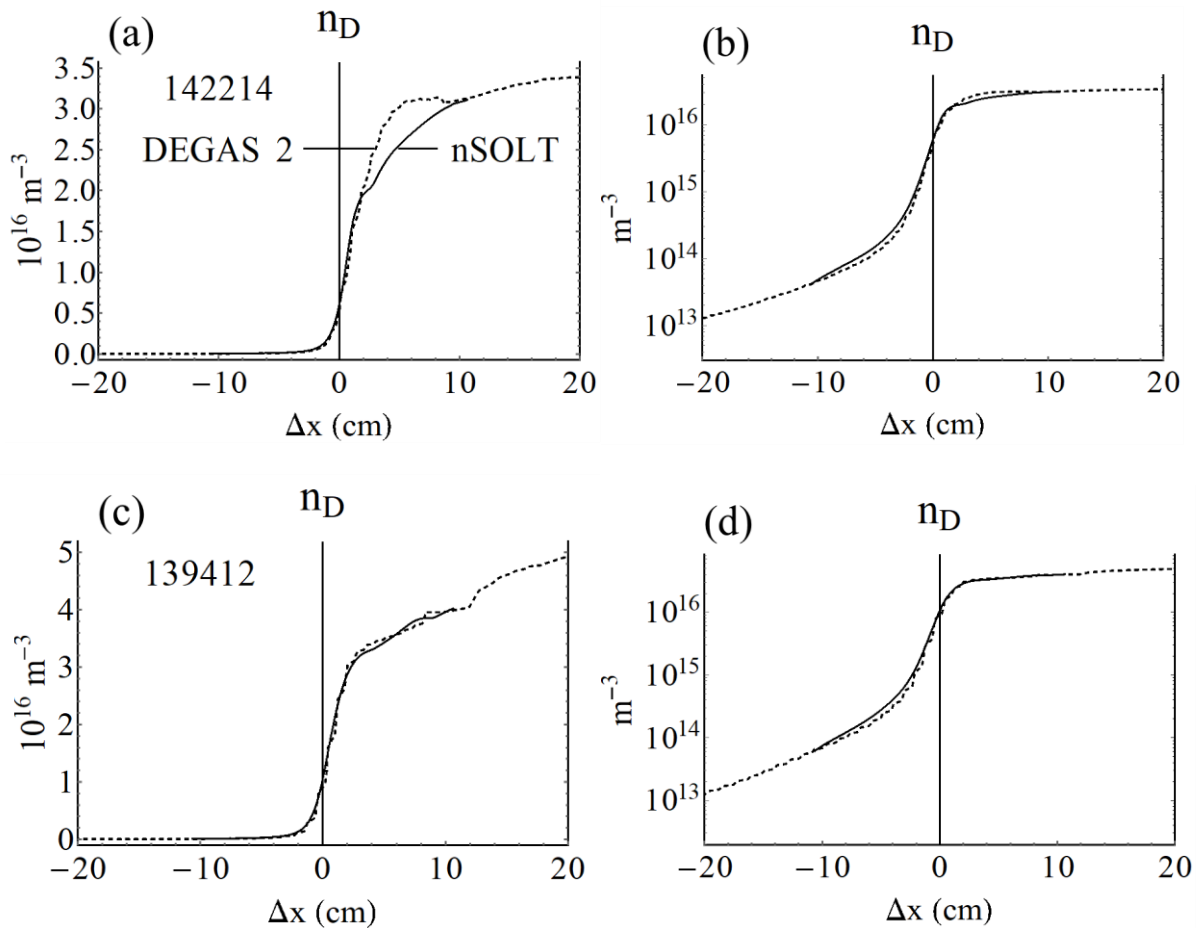


Fig. 2. Neutral atomic deuterium (D) density profiles from DEGAS 2 (dashed) and nSOLT (solid) simulations on linear (a and c) and logarithmic (b and d) scales. nSOLT simulations used puff densities, c.f. Eqs. (3) and (4),  $N = N_0 = 5 \times 10^{16} \text{ m}^{-3}$  and  $6.5 \times 10^{16} \text{ m}^{-3}$  for shots 142214 (a and b) and 139412 (c and d), respectively, to match the DEGAS 2 value of  $n_D$  at the radial boundary of the nSOLT simulations at  $\Delta x = 10.63 \text{ cm}$  ( $x = L_x$ ). [Associated dataset available at <https://doi.org/10.5281/zenodo.1342773>]

Agreement between the D density profiles in Fig. 2 is remarkable in the near-SOL and edge regions. The discrepancy in the mid-SOL, apparent for shot 142214 for  $2 \text{ cm} < \Delta x < 8 \text{ cm}$  in Fig. 2(a), is due to dissociation physics modeled in DEGAS 2 but not in nSOLT.

Dissociation is the only source of D in the DEGAS 2 simulations, and it is distributed throughout the SOL. The discrepancy between the profiles in Fig. 2 (a), is caused by a localized rise in the dissociation rate of  $D_2$ . (There is a constant source of  $D_2$  at the wall in the DEGAS 2 simulations, and the molecules are depleted by dissociation as they propagate into the SOL. See Fig. 11 of reference [28].) There is no such distributed source of D in the nSOLT simulations; the only source is at the simulation boundary at  $\Delta x = 10.63$  cm. That boundary condition, Eq. (3), is the extent of the  $D_2$  dissociation modelling in nSOLT.

A much smaller discrepancy between the profiles is observed in the simulations of shot 139412, shown in Fig. 2(c and d). Comparing the TS profiles for the two shots, Fig. 1, there is a knee in the electron density profile for shot 142214 ( $1 \text{ cm} < \Delta x < 5 \text{ cm}$ ) in comparison with the density profile for shot 139412. This implies a stronger dissociation source that may be responsible for the relative bulge in the DEGAS 2 profile in Fig. 2(a).

Gradient scale lengths ( $\lambda$ ) computed from the profiles of Fig. 2 (a and b) are compared in Fig. 3. Agreement is good in the edge and near-SOL but deteriorates outside of this region. The separation for  $\Delta x > 2$  cm is due to the enhanced dissociation source that drives a larger D density gradient in the DEGAS 2 simulation, as discussed above. The departure for  $\Delta x < -7$  cm is due, in part, to the proximity of the nSOLT boundary condition: there are no neutrals entering from the core-side boundary, but there are neutrals escaping. With the boundary moved from  $\Delta x = -10.63$  cm to  $\Delta x = -31.89$  cm (by doubling the simulation domain at fixed resolution) the roll-over of the gradient scale length moves with it, as demonstrated by the dashed line in Fig. 3. Although the discrepancy in  $\lambda$  grows to about 50% for  $\Delta x < -7$  cm, the density in this region is smaller than at the separatrix by at least two orders of magnitude and is rapidly decreasing; see Fig. 2(b).

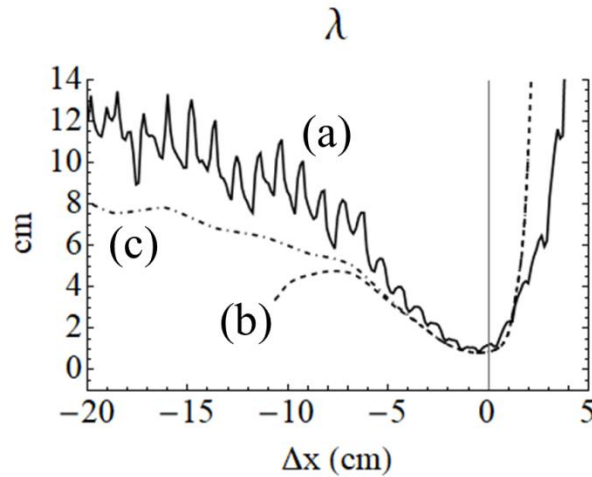


Fig. 3. Density gradient scale length,  $\lambda = (d \ln(n_D) / dx)^{-1}$ , for the DEGAS 2 (a) and nSOLT (b) simulations of shot 142214 corresponding to Fig. 2(a). Curve (c) is for the same nSOLT simulation parameters but on a 2x larger domain with the core-side boundary moved from  $\Delta x = -10.63$  cm to  $\Delta x = -31.89$  cm. The plot is limited to  $-20 \text{ cm} < \Delta x < 5 \text{ cm}$  for clarity. The

wiggles in the DEGAS 2 curve (a) result from a stair-step interpolation of the density. [Associated dataset available at <https://doi.org/10.5281/zenodo.1342773>]

To explore the sensitivity of the density profile to CX physics, in particular the disparity observed in Fig. 3, the DEGAS 2 and nSOLT simulations of shot 142214 were re-run without CX. [It was observed previously in the DEGAS 2 simulations that while the elimination of CX decreased  $n_D$  significantly in the core (viz., decreased the D penetration depth), the gradient scale length was unaffected within a neighborhood of its minimum value, near the separatrix (c.f., Fig. 3). This observation has implications for edge neutral density (ENDD) and gas-puff imaging (GPI) camera diagnostics that depend on atomic emission intensities, [28] and, in part, motivated the following investigation.]

For fixed puff ( $N_0$ ) and  $D_2$  entrance velocity ( $v_{D2}$ ), nSOLT simulations were run for different choices of the Franck-Condon (FC) temperature ( $T_{FC}$ ) in Eq. (3). In the absence of CX, we found that the penetration depth scales with the FC velocity in the nSOLT simulations,

$$v_{FC} = - \int_{-\infty}^0 dv v G(x_{SOL}, v) / \int_{-\infty}^0 dv G(x_{SOL}, v). \quad (9)$$

[ $v_{FC} \sim T_{FC}^{1/2}$ ; see Eq. (3).] This dependence of the penetration depth on the “muzzle velocity” of the puffed neutrals was exploited in the nSOLT simulations to improve agreement between the D density profiles in the core region, where the density is exponentially small. See Fig. 4.

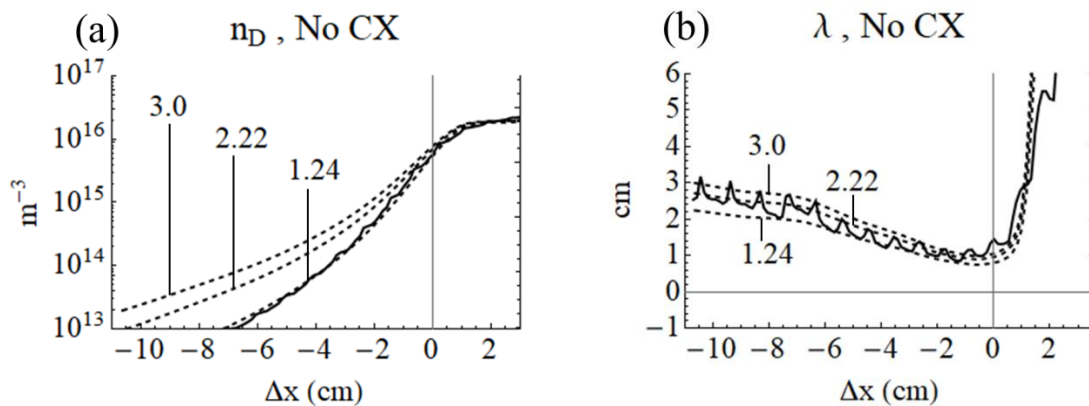


Fig. 4. D density profiles (a) and their gradient scale lengths (b) from DEGAS 2 (solid black) and nSOLT (dashed) simulations of shot 142214, both run without CX physics. The nSOLT simulations are for three different values of the Franck-Condon temperature  $T_{FC}$  (inset, in eV) in Eq. (3). [Associated dataset available at <https://doi.org/10.5281/zenodo.1342773>]

The value of  $T_{FC}$  that gives the best agreement with the DEGAS 2 simulation, 1.24 eV, is significantly less than the 3 eV used in the cases with CX. The difference between the ionization rates was ruled out as a candidate explanation of this disparity by comparing the fit used by nSOLT, Eq. (7), to the tabulated version used in the DEGAS 2 simulation. As

mentioned above, it was found that the ionization rates agree to within 20% over the ranges  $10^{17} \text{ m}^{-3} < n_e < 10^{19} \text{ m}^{-3}$  and  $5 \text{ eV} < T_e < 5 \text{ keV}$ , which includes these simulations, though the electron density is marginal. (See Fig. 1.) Instead, it is believed that the disparity is due to significant differences between the two models in the energetics of D production by dissociation.

The D atoms are not distributed in velocity according to Eq. (3) in the DEGAS 2 simulations, where the distribution function accounts for multiple break-up paths by which  $D_2$  dissociates into D. In addition to the direct 3 eV path, there is a path that involves the molecular ion  $D_2^+$  and results in a 4.3 eV D atom and still other paths that have  $T_e$  - dependent dissociation energies. Suffice it to say: the DEGAS 2 D energy distribution function is not well-modelled by a single-temperature Maxwellian. (See [19] and references therein.) To compensate for the relatively limited dissociation model in nSOLT,  $T_{FC}$  may be regarded as a parameter that can be adjusted in Eq. (3) to improve agreement with the DEGAS 2 D density profiles, particularly for measurements in the tenuous tail of the core-side profile dominated by D in the high-energy tail of the distribution function.

The sensitivity of the core-side gradient scale length ( $\lambda$ ) to  $T_{FC}$  observed in no-CX simulations, Fig. 4(b), is greatly reduced when CX physics is restored to the simulations; three nSOLT simulations corresponding to those depicted in Fig. 4, but *including* CX, showed a negligible dependence of  $\lambda$  on the value of  $T_{FC}$  while, as without CX, the core-side D density increased with  $T_{FC}$ .

The insensitivity of  $\lambda$  to  $T_{FC}$  indicates that CX has thermalized the neutrals with the ions, where the CX rate ( $\sim T_i^{0.3}$ ) grows appreciable in the edge and near-SOL. CX heating of the neutrals is seen in the contour plot of the D energy flux in Fig. 5. To illustrate the observed effect of CX on  $\lambda$ , suppose the ionization mean free path is  $v_{FC} / \langle \sigma v \rangle_{iZ}$  in the SOL and  $v_i / \langle \sigma v \rangle_{iZ}$  in the core, where  $v_{FC}$  is the Franck-Condon velocity corresponding to  $T_{FC}$ , given in Eq. (9), and  $v_i$  is the ion thermal velocity. The density of neutrals reaching the edge from the wall decreases with  $v_{FC}$ , and the density of those continuing into the core falls off exponentially with scale length  $\lambda = v_i / \langle \sigma v \rangle_{iZ}$ , independent of  $v_{FC}$ . In the absence of CX, the scale length is  $\lambda = v_{FC} / \langle \sigma v \rangle_{iZ}$  in the SOL *and* in the core, qualitatively consistent with Fig. 4(b).

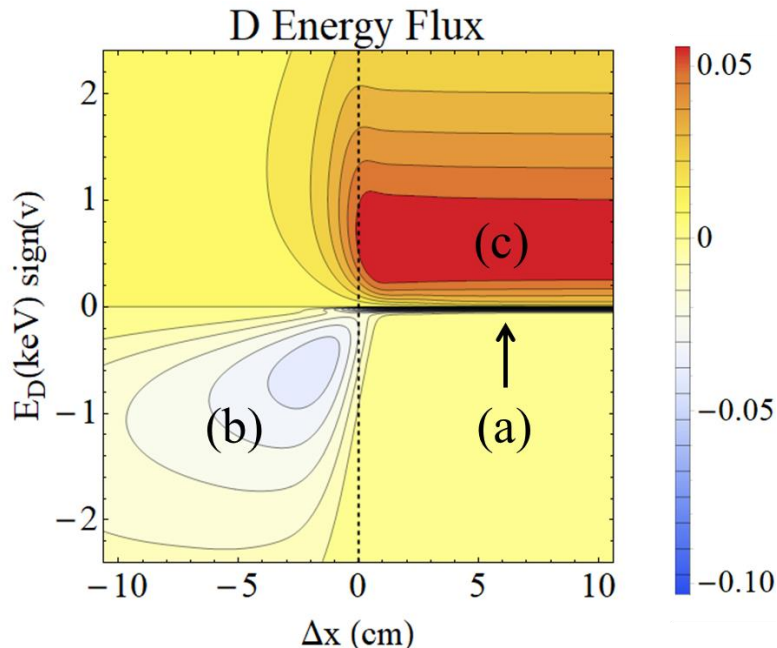


Fig. 5. Contour plot of the local D energy flux divided by the total in-coming ( $v < 0$ ) flux at the wall,  $\Delta v \frac{3}{2} m_D v^3 G(x, v) / (-) \sum_{v < 0} \Delta v \frac{3}{2} m_D v^3 G(x=L_x, v)$ , as a function of radius ( $x$ ) and velocity-signed energy, from the nSOLT simulation of shot 142214. (a) Franck-Condon D atoms injected at the wall stream across the SOL. CX-heated D diffuses into the core (b) and streams across the SOL (c) from the edge. The total in-coming ( $v < 0$ ) energy flux is  $0.39 \text{ kW/m}^2$ , and the total out-going energy flux is  $1.74 \text{ kW/m}^2$ , at the wall. [Associated dataset available at <https://doi.org/10.5281/zenodo.1342773>]

The picture of energy flux in Fig. 5 suggests that injected neutrals free-stream to the edge where they are depleted by ionization and heated by charge exchange. The CX-heated neutrals that continue into the core are consumed by ionization, while those returning to the SOL escape ionization and free-stream back to the wall.

A local mean-free-path analysis helps to identify the deposition domain for the injected neutrals and the origin of heated neutrals reaching the wall. The local D mean-free-paths ( $\lambda_{\text{mfp}}$ ) for CX and IZ are illustrated in Fig. 6 for two choices of velocity corresponding to a) the maximum injected energy flux from the wall, at  $E_D = 15 \text{ eV}$  ( $v < 0$ ), and b) the maximum energy flux reaching the wall from the SOL, at  $E_D = 527 \text{ eV}$  ( $v > 0$ ). (See Fig. 5.)  $\lambda_{\text{mfp}}(x)$  is simply proportional to the velocity ( $v_0$ ) corresponding to  $E_D$ :  $\lambda_{\text{mfp}}(x) = |v_0| / (v_{\text{cx}}, v_{\text{iz}})$ , with the collision rates given by  $v_{\text{cx}} = n_e h_{\text{cx}}$  and  $v_{\text{iz}} = n_e h_{\text{iz}}$ , and with  $h_{\text{cx}}$  and  $h_{\text{iz}}$  given by Eqs. (7) and (8), respectively. In Fig. 6(a), we plot the local attenuation rates ( $1/\lambda_{\text{mfp}}$ ) for the injected  $15 \text{ eV}$  D, and note that the corresponding plot for the  $527 \text{ eV}$  D (not shown) is the same but rescaled by  $(15/527)^{1/2} = 1/6$ . It is seen that attenuation of the injected neutrals grows significant starting at  $\Delta x = 1 \text{ cm}$  and achieves maximum rates for CX and IZ at  $\Delta x = -2 \text{ cm}$  and  $-1.5 \text{ cm}$ , respectively.

This suggests a common domain for the deposition of injected D and for the origin of CX-heated D, viz.,  $-2 \text{ cm} < \Delta x < 1 \text{ cm}$ , consistent with Fig. 5.

The horizontal contour lines in the SOL ( $v > 0$ ) of Fig. 5 suggest that CX-heated D is free-streaming to the wall directly from the edge region, and the local  $\lambda_{\text{mfp}}(x)$  profile enforces this observation. We plot the distance to the wall minus  $\lambda_{\text{mfp}}(x)$  for the 527 eV D in Fig. 6(b) and cut the plot off where that difference is negative, i.e., where the mean free path is greater than the distance to the wall. It is seen that all 527 eV (and greater) D that enter the SOL free-stream to the wall.

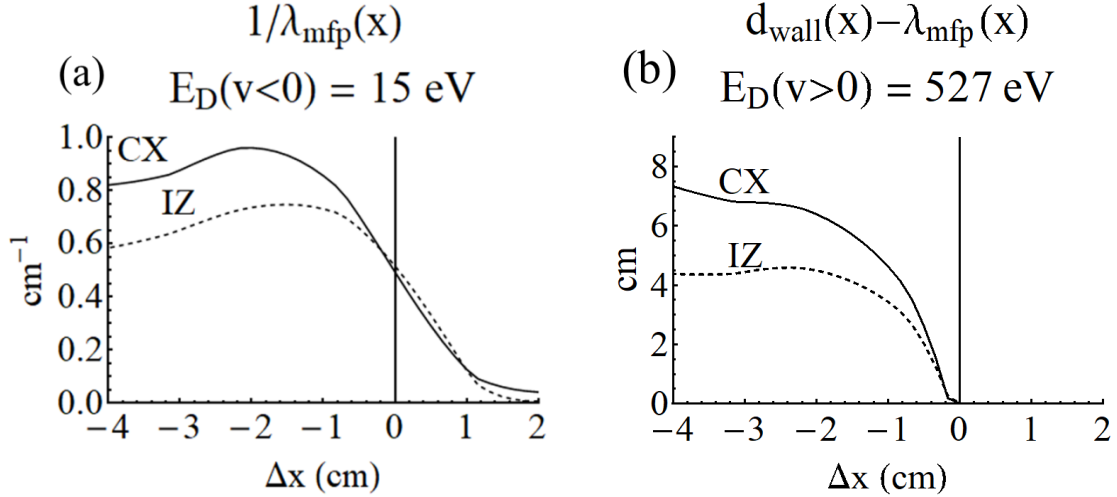


Fig. 6. For the local mean-free-path,  $\lambda_{\text{mfp}}(x) = |v_0| / (v_{\text{cx}}, v_{\text{iz}})$ : (a)  $1/\lambda_{\text{mfp}}(x)$  for the velocity at which the injected D energy flux from the wall is maximized ( $E_D = 15 \text{ eV}$ ,  $v_0 = -22 \text{ km/sec}$ ) and (b) the distance from  $x$  to the wall,  $d_{\text{wall}}(x) = L_x - x$ , minus  $\lambda_{\text{mfp}}(x)$  for the velocity at which the CX-heated D energy flux from the edge is maximized at the wall ( $E_D = 527 \text{ eV}$ ,  $v_0 = 130 \text{ km/sec}$ ). The collision rates are given by  $v_{\text{cx}} = n_e h_{\text{cx}}$  and  $v_{\text{iz}} = n_e h_{\text{iz}}$ , with  $h_{\text{cx}}$  and  $h_{\text{iz}}$  given by Eqs. (7) and (8), respectively. The plasma profiles are from the nSOLT simulation of shot 142214. [Associated dataset available at <https://doi.org/10.5281/zenodo.1342773>]

#### IV. 1D neutral-plasma evolution in nSOLT

Encouraged by the agreement between DEGAS 2 and nSOLT simulations for fixed plasma profiles, described in Sec. III, we take the logical next step and allow the plasma to evolve self-consistently with the neutrals in nSOLT but restrict the plasma evolution to 1D, using radial diffusion as a proxy for turbulent transport. The model solved here consists of Eqs. 1 and the 1D version of Eqs. 2 which is given explicitly in the appendix (A5). We do not impose  $T_i = T_e$  here as we did in Sec. III.

In Sec. III our goal was to demonstrate that the neutral evolution model in nSOLT can recover the neutral profile obtained by DEGAS 2 simulations for two particular H-mode shots on NSTX for which detailed data concerning the distribution of the neutral species was available. Our goal in the present section is to demonstrate that the simulations can recover, self-consistently and with appropriate neutral fueling at the far-SOL boundary, values of plasma density and temperature observed for a class of discharges, rather than for a particular shot. The physical parameters used in the simulations are typical of Ohmic L-mode shots on NSTX, for which a large data base and considerable analysis is available.[30]

Self-consistent steady states, sustained by neutral gas puffing at the far-SOL boundary ( $N_0 > 0$ ,  $R_0 = 0$  and  $R_i = 0$  in Eq. 4) and plasma heating in the core ( $S_n = 0$ ,  $S_{Pe} > 0$  and  $S_{Pi} > 0$  in Eqs. 2), are reached in the simulations on millisecond time scales for the NSTX parameters. The approach to equilibrium is illustrated in Fig. 7. Included in the figure are earlier histories of  $n_e$  and  $T_e$  for a simulation that reached equilibrium sustained by direct injection of plasma in the core ( $S_n > 0$ ) and without neutrals ( $N_0 = 0$ ). That equilibrium was used as the initial condition for the appended simulation with no direct injection in the core ( $S_n = 0$ ) and with neutral puff injection at the wall ( $N_0 = 5 \times 10^{11} \text{ cm}^{-3}$ ). In other words,  $S_n$  was turned off and the puff was turned on at  $t = 7$  ms. The fixed source  $S_n$  (for  $t < 7$  ms) and the ionization source  $h_{iz}n_0n_e$  (plotted for the steady state reached in the puff-driven case,  $t > 7$  ms) are plotted in Fig. 8.

The injection of plasma particles and energy by fixed sources in these 1D diffusive simulations requires further description. Focusing on the density, with similar remarks holding for the ion and electron energy injection, the source function  $S_n(x)$  is a Gaussian contained within a core-side “buffer zone.” The diffusion coefficient  $D_n(x)$  is larger in the buffer zone than it is in the edge and SOL. (See Fig. 8.) The radial density gradient is held to zero on the core-side boundary ( $\Delta x = -10.63$  cm), so the diffusive flux there is zero, regardless of the diffusion coefficient. However, a sufficiently large, and perhaps unphysical, value of  $D_n$  will keep the density flat in the buffer zone, despite the presence of the localized source, and so render the flux into the edge region ( $\Delta x > -5$  cm) independent of the location of the source, as in these simulations. (In turbulence simulations, not reported here, the large diffusion coefficient keeps negative fluctuations, i.e. holes, from reaching the boundary where, otherwise, they can coalesce in large vorticity cells.) Thus the location and width of  $S_n(x)$  are ad hoc in these simulations and were fixed as indicated in Fig. 8.

We control the flux of particles entering the edge from the core by adjusting  $S_n$  for a particular choice of  $D_n$  in the buffer zone, and we control the flux of particles in the edge and

SOL regions ( $\Delta x > -5$  cm) by adjusting the smaller, more physical value of  $D_n$  in those regions. The value of  $D_n$  in the edge and SOL controls the “turbulent” transport there, by proxy, and is either  $3 \text{ m}^2/\text{sec}$  or  $30 \text{ m}^2/\text{sec}$ , as indicated in the figure captions in this section of the paper.

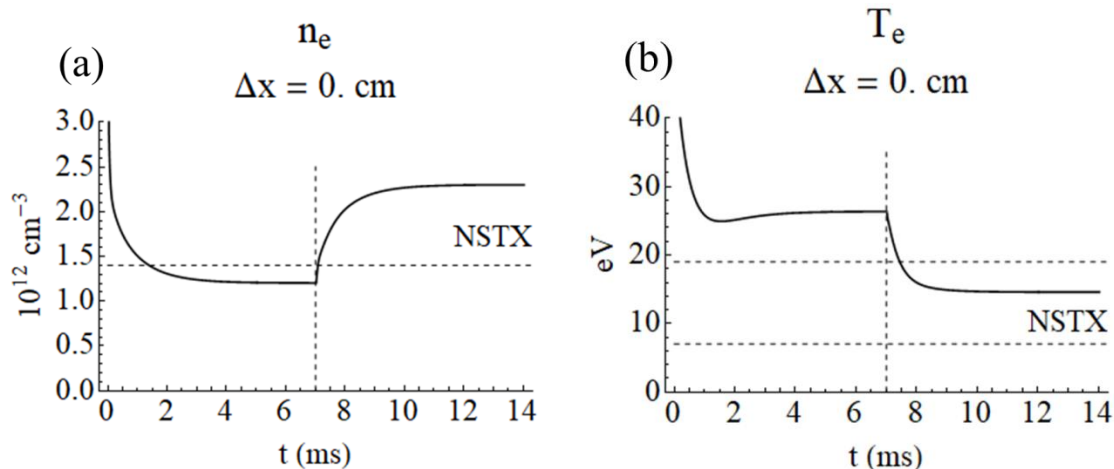


Fig. 7. Electron density (a) and temperature (b) histories at the separatrix from two nSOLT simulations: the first ( $0 \text{ ms} < t < 7 \text{ ms}$ ) was fueled by direct plasma injection in the core and no neutrals ( $S_n > 0$  and  $N_0 = 0$ ); the second ( $7 \text{ ms} < t < 14 \text{ ms}$ ) continued with  $S_n = 0$  and  $N_0 = 5 \times 10^{11} \text{ cm}^{-3}$ . In both cases,  $D_n = 3 \text{ m}^2/\text{sec}$  and  $D_{Pe} = D_{Pi} = 30 \text{ m}^2/\text{sec}$ , in the edge and SOL, and the maximum core-side heating rates are  $S_{Pe} = 0.65 \text{ MW}/\text{m}^3$  and  $S_{Pi} = 6.5 \text{ MW}/\text{m}^3$ . The dashed horizontal lines bound the ranges observed in Ohmic L-mode shots on NSTX for a large dataset [30]; the upper bound in (a) is off the graph at  $6 \times 10^{12} \text{ cm}^{-3}$ . [Associated dataset available at <https://doi.org/10.5281/zenodo.1342773>]

No attempt was made to adjust the particle sources,  $S_n$  and  $h_{iz}n_0n_e$ , to give the same initial and final states in the simulations depicted in Figs. 7 and 8. That is impossible, *a priori*, because the ionization source depends on the evolving fields. Indeed it is this self-consistency of neutral source and plasma profiles that motivated the nSOLT development. It is simply to be noted that equilibrium density and temperature profiles typical of NSTX Ohmic L-mode shots can be obtained either by direct injection in the core or by neutral fueling at the wall, and that similar plasma profiles are obtained for sources that are alike in magnitude while differing in radial distribution.

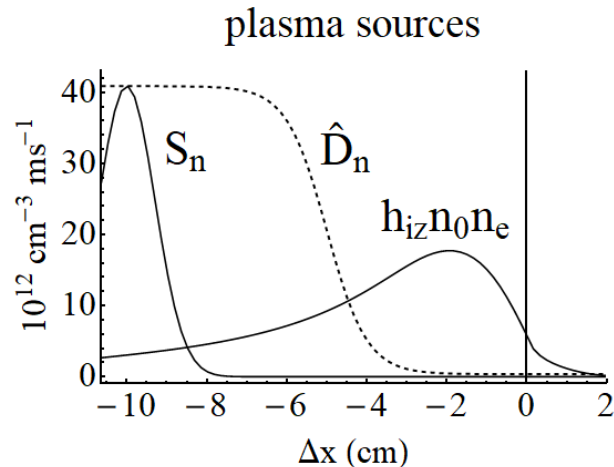


Fig. 8. Plasma particle sources,  $S_n$  and  $h_{iz}n_0n_e$ , for the simulations of Fig. 7.  $S_n$  is a constant source that is non-zero only for  $0 \text{ ms} < t < 7 \text{ ms}$  in the simulations of Fig. 7. The ionization source,  $h_{iz}n_0n_e$ , is non-zero only for  $7 \text{ ms} < t < 14 \text{ ms}$ , and is plotted here for the equilibrium reached at the end of the puff-driven simulation ( $t = 14 \text{ ms}$ ) in Fig. 7. The dimensionless density diffusion coefficient  $\hat{D}_n$  is also plotted (dashed), re-scaled to fit in the plot frame with the sources which are plotted in the units indicated on the vertical axis. [Associated dataset available at <https://doi.org/10.5281/zenodo.1342773>]

Figure 9 summarizes results from ten nSOLT simulations fueled by neutral puffing at the wall and with no direct plasma injection in the core, as in the simulation depicted in Fig. 7 for  $t > 7 \text{ ms}$ . A scan of five puff densities ( $N_0$ ) and two values of the plasma density diffusion coefficient ( $D_n$ ) was performed, with the higher (lower)  $D_n$  values corresponding, by proxy, to stronger (weaker) turbulent transport. The electron density rises, and the electron temperature falls, with increasing puff density. Stronger transport ( $D_n$ ) removes density to the SOL where it drains away along open field lines, requiring stronger neutral fueling to sustain it within prescribed limits, as seen in Fig. 9(a). The increase in  $T_e$  with  $D_n$ , apparent in Fig. 9(b) at the lower values of  $N_0$ , is caused by the decrease in  $n_e$  with stronger transport; the plasma is heated by constant sources of energy density ( $S_{Pe}$  and  $S_{Pi}$ ), so the sources of energy per particle ( $T_e$  and  $T_i$ ) are inversely proportional to the density. See Eqs. 2(b and c).

Equilibria typical of H-mode discharges on NSTX have been found as well, by increasing the puff density and the electron heating from the values used in these Ohmic L-mode simulations, and will be described in a future publication.

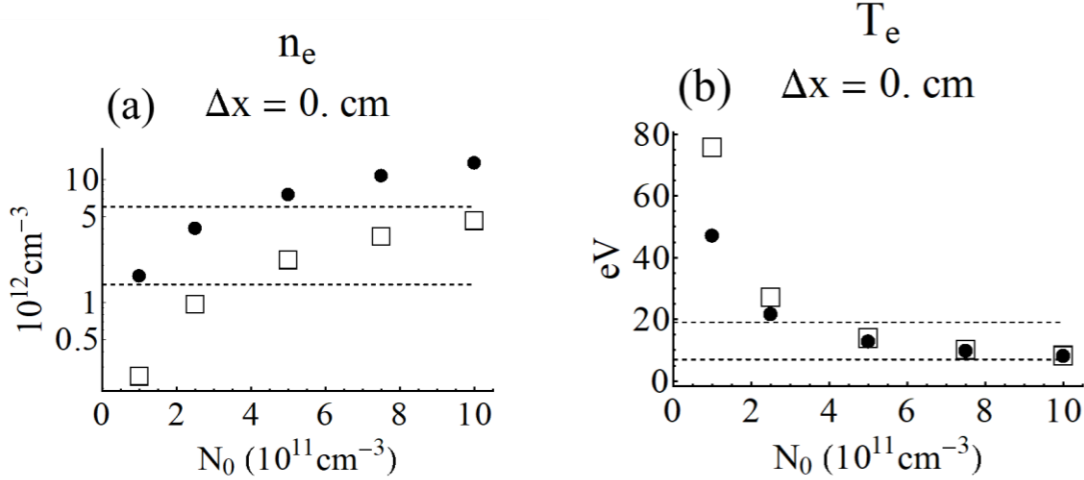


Fig. 9. Electron density (a) and temperature (b) at the separatrix as functions of the puff density ( $N_0$ ) from nSOLT simulations in steady state for two values of the density diffusion coefficient:  $D_n = 0.3 \text{ m}^2/\text{sec}$  (solid dots) and  $3.0 \text{ m}^2/\text{sec}$  (open squares).  $D_{Pe} = D_{Pi} = 30 \text{ m}^2/\text{sec}$ , in the edge and SOL, and the maximum core-side heating rates are  $S_{Pe} = 0.65 \text{ MW}/\text{m}^3$  and  $S_{Pi} = 6.5 \text{ MW}/\text{m}^3$ , as in Fig. 7. The dashed horizontal lines bound the ranges observed in a published database of Ohmic L-mode shots on NSTX.[30] [Associated dataset available at <https://doi.org/10.5281/zenodo.1342773>]

Turning to the mean flows, the neutrals reduce the mean  $E \times B$  flow speed and its shearing rate, consistent with previous observations from XGC1 simulations, [2] as seen in Fig. 10. Prior SOLT simulations [9] found mean flows in the SOL that were greater in magnitude than those inferred from GPI diagnostics on NSTX. The simulated flows could be brought into agreement with the GPI data by introducing ad hoc vorticity dissipation, and it was hoped that the same encouraging result might be obtained with more realistic neutral friction modelling. However, when the simulations here were repeated without the neutral friction, Eq. (2f), in the vorticity evolution, the results of Figs. 9 and 10 were negligibly altered; the flow and shearing rate reductions observed in Fig. 10 are primarily the result of decreasing plasma temperature gradient in the SOL with increasing  $N_0$ . The minimum velocity, i.e., the largest negative velocity in the SOL, Fig. 10(a), occurs as the parallel connection length decreases with increasing radius, tending to enforce sheath-dominated potentials having  $\phi \cong \phi_B = 3T_e(x)$  and  $v_{Ey} \cong \partial_x \phi_B = 3\partial_x T_e(x)$ . [31] Ionization reduces the electron temperature gradient, and sheath physics consequently reduces the flow and the flow shearing rate. The electron temperature gradient and  $v_{Ey}$  are compared in Fig. 11 for three of the cases in Figs. 9 and 10.

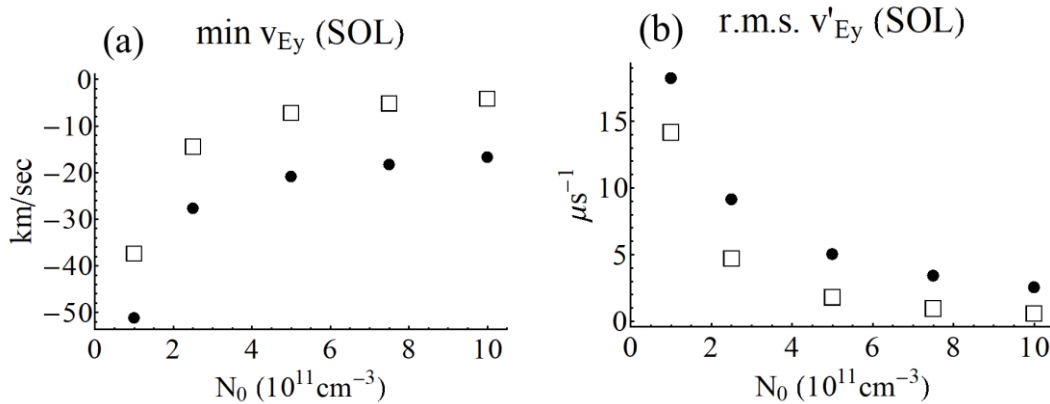


Fig. 10. The maximum negative poloidal  $E \times B$  velocity ( $v_{Ey}$ ) measured in the SOL (a) and the root-mean-square (r.m.s.) shearing rate ( $v'_{Ey}$ ) of that flow over the SOL (b), as functions of  $N_0$ , for the nSOLT simulations of Fig. 9. [Associated dataset available at <https://doi.org/10.5281/zenodo.1342773>]

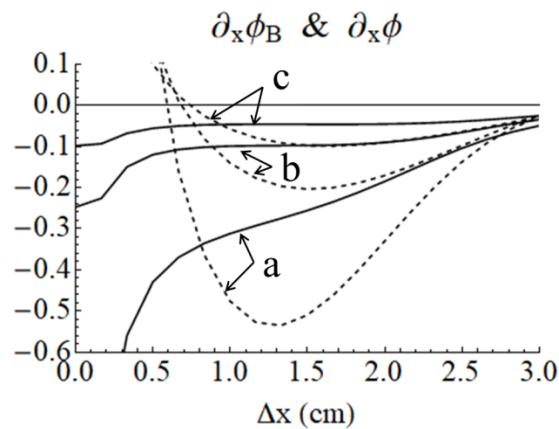


Fig. 11. The radial gradients of  $\phi_B$  (solid) and of  $\phi$  (dashed) in the SOL for  $N_0 = 1$  (a),  $2.5$  (b) and  $5$  (c)  $\times 10^{11} \text{ cm}^{-3}$  and all for  $D_n = 3.0 \text{ m}^2/\text{sec}$ , i.e., the left-most three boxes in Figs. 9 and 10.  $\phi_B = 3T_e$  is the Bohm potential and  $\partial_x \phi = v_{Ey}$ , the poloidal  $E \times B$  velocity. [Associated dataset available at <https://doi.org/10.5281/zenodo.1342773>]

Profiles of the mean flows for  $N_0 = 5 \times 10^{11} \text{ cm}^{-3}$  and  $D_n = 3.0 \text{ m}^2/\text{sec}$  (the open box in the middle of Figs. 9 and 10) are shown in Fig. 12. Notice that  $v_{Ey} + v_{diy} \cong 0$ , i.e., the  $E \times B$  and ion diamagnetic flows are nearly “mirrored” in the core region ( $\Delta x < 0$ ). Mirroring could sustain sheared-flow suppression of the interchange instability with a growing ion pressure gradient [ $v_{Ey}' = -v_{diy}' = -(P_i'/n)'$ ] and so enhance access to a durable H-mode. [32] In the present simulations, damping of the total flow, by CX friction and vorticity diffusion, encourages the formation of mirrored flows in the core.

In these 1D simulations ( $\partial_y = 0$ ), the vorticity evolution equation (2d) reduces to

$$\partial_t \rho = \partial_x^2 (D_\rho \rho) - \partial_x f_y - \nabla_{//} j_{//} ,$$

or, using (2e) and (2f) and integrating once in  $x$ , to

$$\partial_t n v_T = \partial_x [D_\rho \partial_x n v_T] - v_{cx} n v_T + (v_{cx} + v_{iz}) n v_{0y} + \int^x dx' \nabla_{//} j_{//} , \quad (10)$$

where  $n v_T = n(v_{Ey} + v_{diy})$ ,  $v_{cx} = h_{cx} n_0$  and  $v_{iz} = h_{iz} n_0$ . On the closed flux surfaces ( $\Delta x < 0$ ), the parallel current density is purely a fluctuation, [27] of which there are none in 1D, so  $\nabla_{//} j_{//} = 0$ . Thus, to within a (generally small) correction from the neutral flow ( $v_{0y}$ ), mirrored flows ( $v_T = 0$ ) are an equilibrium solution ( $\partial_t = 0$ ) of Eq. (10) in the core. In the SOL, however,  $\nabla_{//} j_{//}$  is determined by sheath physics and is not ignorable. Furthermore, to the extent that the SOL is electrically connected to the sheath,  $v_{Ey}$  is determined by the Bohm potential,  $v_{Ey} \cong \partial_x \phi_B = 3 \partial_x T_e$ , and is negative, in general, as is  $v_{di} = P_i'/n$ , precluding mirrored flows. The transition from  $v_{diy}$ -mirrored to sheath-dominated  $v_{Ey}$  is apparent in Fig. 12.

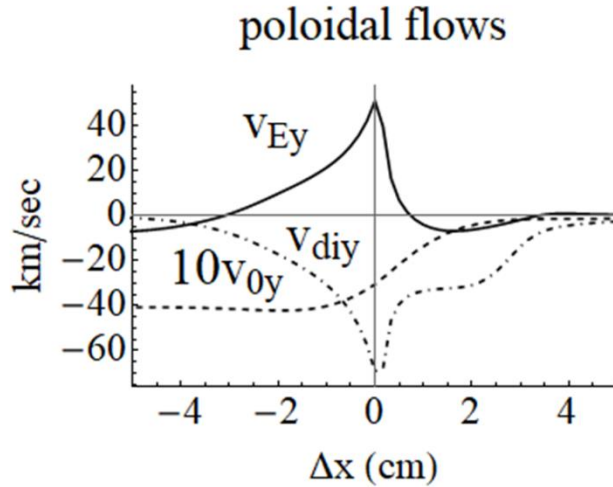


Fig. 12. Mean flow profiles for the simulation with  $N_0 = 5 \times 10^{11} \text{ cm}^{-3}$  and  $D_n = 3.0 \text{ m}^2/\text{sec}$  (the middle square in Figs. 9 and 10). Notice that  $10v_{0y}$  is plotted. [Associated dataset available at <https://doi.org/10.5281/zenodo.1342773>]

Earlier simulations also led us to suspect that the flow shearing rates were large enough to drive the Kelvin-Helmholtz (K-H) instability in the edge region [33] and so to threaten access to a sustained H-mode. Although neutrals may enable such access by reducing the K-H growth rate ( $\sim |v'_{Ey}|$ ), the reduced velocity shear may likewise allow an otherwise suppressed interchange instability if the interchange growth rate exceeds the flow shearing rate. [34] The study of the

effects of neutrals on plasma instabilities requires 2D analysis and turbulence simulations and will be pursued in the future.

## V. Concluding remarks

We have extended the 2D SOLT model of plasma turbulence in the SOL to include interaction with neutral atoms, resulting in a new code called “nSOLT.” The neutrals are evolved in 1D ( $x, v_x$ ) by a radial Boltzmann equation, including charge exchange and ionization physics, in which interaction with the plasma is represented by its bi-directionally ( $y$ ) averaged fields.

As a first verification exercise, we compared neutral deuterium density profiles obtained from kinetic Monte Carlo (DEGAS 2) simulations to those obtained from nSOLT simulations for fixed plasma density and temperature profiles measured on two NSTX H-mode discharges. Aligning the nSOLT and DEGAS 2 neutral densities at a point in the far-SOL led to good agreement between the time-asymptotic equilibrium neutral profiles throughout the SOL and edge regions. Discrepancies were attributed to the volume-distributed molecular ( $D_2$ ) dissociation source of D in DEGAS 2, compared to the simple boundary influx of Franck-Condon D in nSOLT.

Comparing nSOLT and DEGAS 2 simulations conducted with and without CX collisions confirmed the observation from earlier DEGAS 2 simulations [28] that, within a neighborhood of its minimum value in the edge region, the neutral gradient scale length is insensitive to CX physics. That is, the most rapid fall-off of the neutral density is predominantly due to ionization. In the nSOLT simulations without CX, the neutral penetration depth scaled with the Franck-Condon velocity ( $v_{FC} \sim T_{FC}^{1/2}$ ), and it was found that a value of  $T_{FC}$  significantly lower than the canonical 3 eV was necessary in order to match the DEGAS 2 profile obtained without CX. Drawing physical implications from this result is difficult due to multiple spikes in the distribution of deuterium velocities in DEGAS 2 simulations that correspond to different molecular dissociation paths included in the model. The single Maxwellian distribution function used in nSOLT cannot account for the richness of this velocity distribution, and  $T_{FC}$  must be regarded as a free parameter that can be adjusted to align the neutral density profiles, particularly where they are exponentially small deeper in the edge region.

In these simulations, the sensitivity of the neutral penetration depth to  $T_{FC}$  is lost in the presence of CX which thermalizes the neutrals with the ions in the edge region, effectively giving them the ion thermal speed and a penetration depth ( $v_i / n_i h_{iz}$ ) independent of  $T_{FC}$ . Contour plots of the neutral energy flux in phase space and a local MFP analysis were used to locate the deposition zone of cold ( $T_{FC}$ ) neutrals injected from the wall, and the birth zone of CX-heated neutrals returning to the wall.

As a first illustration of the self-consistent neutral-plasma evolution in nSOLT, we performed 1D simulations in which linear diffusion served as a proxy for turbulent transport. By adjusting the neutral fueling (“puff”) density at the wall, and with no other source of plasma

particles, we found time-asymptotic equilibria with electron densities and temperatures typical of Ohmic L-mode shots on NSTX. Flow damping by neutral friction was found to be negligible compared to the flow reduction brought about by electron temperature profile modification due to ionization in these simulations; ionization reduces the temperature gradient, and sheath physics ( $\phi \sim \phi_B = 3T_e$ ) serves to reduce the mean poloidal  $E \times B$  flow ( $v_{E\theta} = \partial_x \phi$ ) in the SOL. It was observed that the flow reduction could lead to improved agreement between mean poloidal flows measured by GPI diagnostics on NSTX and those observed previously in SOLT simulations. Neutral friction encourages the formation of mirrored  $E \times B$  and ion diamagnetic flows in the edge and so may provide access to a durable H-mode, as the  $E \times B$  flow shearing rate grows with the ion pressure gradient in the mirrored state. But the friction profile also depends on sheath physics in the near-SOL. Thus, neutrals are expected to be important for establishing confinement-enhancing flows in the edge and a link between conditions at the divertor and those flows. Questions concerning confinement, e.g., instability suppression by neutral friction, will be pursued with the 2D-turbulence version of nSOLT.

In conclusion, it is seen that the reduced neutral kinetic model presented here may provide economical and reasonably accurate simulations that couple plasma and neutral profiles in the edge region. Such coupled-profile models will be essential to investigate quasi-steady turbulent states in the edge and SOL regions with self-consistent particle sources and hence to enable increasingly realistic modelling of edge and SOL profiles, neutral and plasma fluxes to the wall, and edge plasma confinement modes.

## Acknowledgments

This material is based upon work supported by the US Department of Energy Office of Science, Office of Fusion Energy Sciences under award numbers DE-FG02-97ER54392 and DE-AC02-09CH11466.

## Appendix: neutral-plasma interaction model equations

In section A1 we derive the 1D neutral kinetic model, Eqs. (1), from the 3D Boltzmann equation including charge exchange and ionization collision integrals. In A2 we derive expressions for the terms describing neutral interactions in the plasma evolution equations, Eqs. (2), that are added to the SOLT model. A discussion of momentum and energy conservation is given in A3. A note on our neglect of radiative recombination in the model is given in A4, and the explicit form of the plasma evolution equations in 1D, solved in Sec. IV of the main text, is given in A5.

A1. A 1D Boltzmann model for the neutral evolution

Let the 3D ion and neutral distribution functions be denoted by  $f$  and  $g$  respectively. In the presence of charge exchange and ionizing collisions, the Boltzmann equations [35] for  $f$  and  $g$  are

$$\partial_t f + \mathbf{v} \cdot \nabla_x f = -X(f, g) + h_{iz} n_e g \quad (\text{A.1})$$

and

$$\partial_t g + \mathbf{v} \cdot \nabla_x g = X(f, g) - h_{iz} n_e g \quad (\text{A.2})$$

where

$$X(f, g) = \int d^3 v' \sigma_{cx}(\mathbf{v}, \mathbf{v}') |\mathbf{v} - \mathbf{v}'| [f(\mathbf{v})g(\mathbf{v}') - f(\mathbf{v}')g(\mathbf{v})] \quad (\text{A.3})$$

and  $\sigma_{cx}$  denotes the cross section for the CX collision. We have suppressed Coulomb collision and acceleration ( $\mathbf{a} \cdot \nabla_v f$ ) terms in (A.1) to focus attention on the neutral interactions. There is no acceleration term for neutrals because there is no mean force acting on the neutrals. We ignore neutral-neutral collisions and radiative recombination.

In (A.1) and (A.2) we have reduced the ionization collision integral, similar in form to the CX integral (A.3), by neglecting the neutral thermal velocity compared to the electron thermal velocity and replacing  $\sigma_{iz}(\mathbf{v})|\mathbf{v}|$  by its average (“ $\langle \sigma_{iz} v \rangle$ ”) over the assumed Maxwellian electron distribution function, [36] so the integral over  $\mathbf{v}'$  reduces to the electron number density,  $n_e = \int d^3 v' f_e(\mathbf{v}')$ . This average ionization rate per particle,  $\langle \sigma_{iz} v \rangle \equiv h_{iz}(T_e)$ , is a function of the electron temperature and is given explicitly in Sec. III.

To simplify (A.3) similarly, we follow Hazeltine et al. [35] and assume that  $\sigma_{cx}(\mathbf{v}, \mathbf{v}')|\mathbf{v} - \mathbf{v}'|$  is approximately independent of the relative velocity and replace it with its average over the Maxwellian ion distribution function. This average CX rate per particle,  $\langle \sigma_{cx} v \rangle \equiv h_{cx}(T_i)$ , depends weakly on the ion temperature, and the expression assumed for it in the simulations is given explicitly in Sec. III. (Other authors take the cross section  $\sigma_{cx}(\mathbf{v}, \mathbf{v}')$  to be constant, [36] and retain the relative velocity  $|\mathbf{v} - \mathbf{v}'|$  without further approximation in the integrand.) We note that the expression given in Eq. (8) breaks down at small  $T_i$  or large  $E_0$  because it assumes that the ion energy is greater than the neutral energy.

To model the neutral dynamics, in which the neutrals interact with the plasma only through the y-averaged plasma fields, we assume a mean-field ion distribution function ( $\tilde{f}$ ) of the form

$$\tilde{f} = \bar{n}_i \exp \left[ -(\mathbf{v}_x^2 + (\mathbf{v}_y - \bar{v}_{iy})^2 + \mathbf{v}_z^2) / 2\bar{T}_i \right] / (2\pi\bar{T}_i)^{3/2}, \quad (\text{A.4})$$

where the over-bar denotes the y-average, and  $\bar{v}_{iy}$  is the sum of  $E \times B$  and ion diamagnetic mean flows. Similarly we replace  $T_e$  and  $T_i$  with their poloidal averages in  $h_{iz}$  and  $h_{cx}$ . With these replacements, the y-averaged neutral Boltzmann equation is

$$\partial_t \bar{g} + \partial_x (v_x \bar{g}) = h_{cx} \left[ \tilde{f} \int dv^3 \bar{g} - \bar{g} \bar{n}_i \right] - h_{iz} \bar{n}_e \bar{g}, \quad (\text{A.5})$$

where we assume periodic boundary conditions in  $y$  and no toroidal dependence.

Integrating (A.5) over  $(v_y, v_z)$  yields the evolution model for the 1D neutral distribution function ( $G$ ),

$$\partial_t G + \partial_x (v_x G) = h_{cx} [F n_0 - G \bar{n}_i] - h_{iz} \bar{n}_e G \quad (\text{A.6})$$

where

$$G = \int dv_y dv_z \bar{g}, \quad (\text{A.7})$$

$$F = \bar{n}_i \exp \left[ -v_x^2 / (2\bar{T}_i) \right] / (2\pi\bar{T}_i)^{1/2}, \quad (\text{A.8})$$

and

$$n_0 = \int dv_x G. \quad (\text{A.9})$$

In order to describe the self-consistent neutral drag of the mean (binormal) plasma flows, we require an evolution equation for the  $y$ -component of the neutral fluid velocity. The density moment of (A.5) is (with no volume source of neutrals in the present formulation)

$$\partial_t n_0 + \partial_x (n_0 v_{0x}) = -h_{iz} \bar{n}_e n_0 \quad (\text{A.10})$$

and the  $v_y$  moment is

$$\partial_t (n_0 v_{0y}) + \partial_x \left( \int dv^3 v_x v_y \bar{g} \right) = \bar{n}_i n_0 h_{cx} \left[ \bar{v}_{iy} - v_{0y} \right] - h_{iz} \bar{n}_e n_0 v_{0y}, \quad (\text{A.11})$$

where  $n_0 v_{0(x,y)} = \int dv^3 v_{(x,y)} \bar{g}$ , and the mean ion fluid velocity is the sum of the  $E \times B$  and ion diamagnetic velocities,  $\bar{v}_i = \bar{v}_E + \bar{v}_{di}$ . In (A.11) we assume that the neutral source does not inject momentum, i.e. the neutrals are introduced at zero mean velocity. Combining (A.10) and (A.11), we find

$$\partial_t v_{0y} = h_{cx} \bar{n}_i (\bar{v}_{iy} - v_{0y}) + v_{0y} \partial_x (n_0 v_{0x}) / n_0 - \partial_x \left( \int dv^3 v_x v_y \bar{g} \right) / n_0. \quad (\text{A.12})$$

While the flux  $n_0 v_{0x}$  in (A.12) is calculated from  $G$ , we require a closure ansatz for the last term, and we choose  $\int d^3v v_x v_y \bar{g} = n_0 v_{0x} v_{0y}$ . With this choice, the result

$$\partial_t v_{0y} + v_{0x} \partial_x v_{0y} = h_{cx} \bar{n}_i (\bar{v}_{iy} - v_{0y}) \quad (\text{A.13})$$

has the form of a radial advection equation for  $v_{0y}$ , in the presence of a “friction” force due to charge-exchange.

Equations (A.6) and (A.13) comprise the neutral evolution equations in the nSOLT model, viz., equations 1(a) and 1(b) in Sec. II.

## A2. Plasma evolution due to neutral interactions

The additional terms to be added to the plasma evolution equations follow from the velocity moments of the ion Boltzmann equation (A.1) but with the CX and IZ rates represented by their mean values, as described above, and the neutrals by the 1D distribution function  $G$ . The density, velocity and energy moments of (A.1), using (A.3), are

$$\partial_t n_{(i, e)} = h_{iz} n_e n_0 + \dots, \quad (\text{A.14})$$

$$\partial_t (n_i \mathbf{v}_i) = h_{cx} n_i n_0 (\mathbf{v}_0 - \mathbf{v}_i) + h_{iz} n_e n_0 \mathbf{v}_0 + \dots, \quad (\text{A.15})$$

and

$$\partial_t \frac{3}{2} n_i T_i = -h_{cx} n_i n_0 \left( \frac{3}{2} T_i - E_0 \right) + h_{iz} n_e n_0 E_0 + \dots, \quad (\text{A.16})$$

where

$$\int d\mathbf{v}^3 f = n_i, \quad (\text{A.17})$$

$$\int d\mathbf{v}^3 \mathbf{v} f = n_i \mathbf{v}_i, \quad (\text{A.18})$$

$$\int d\mathbf{v}^3 \frac{1}{2} v^2 f = \frac{3}{2} n_i T_i, \quad (\text{A.19})$$

and

$$\int d\mathbf{v}^3 \frac{1}{2} v^2 g = \frac{1}{2} \alpha^2 \int d\mathbf{v}_x v_x^2 G = n_0 E_0. \quad (\text{A.20})$$

The ellipsis (...) represents the evolution without neutral interactions, i.e., the original SOLT model terms. Electron and ion densities increase at the same rate in order to preserve quasi-neutrality in (A.14). We have introduced an isotropy parameter  $\alpha^2$  to relate the 1D and 3D energy densities in (A.20);  $\alpha^2 = 1$  corresponds to cold neutrals in  $(v_y, v_z)$ , and  $\alpha^2 = 3$  to

isotropic neutrals with temperature  $2/3E_0$ . Notice that CX works to establish the isotropic equilibrium  $E_0 = 3/2T_i$  in (A.16).

Ionization also affects the electron energy. The average energy loss per ionization ( $E_{iz}$ ) includes the ionization energy itself (13.6 eV for D) plus a factor which accounts for the probability of electron impacts causing atomic level shifts plus radiation (unless these are explicitly accounted for by a radiation term). [37] The electron energy equation is

$$\partial_t \frac{3}{2} n_e T_e = -h_{iz} n_e n_0 E_{iz} + \dots \quad (\text{A.21})$$

Typical values of  $E_{iz}$  range from one to three times the atomic ionization energy, or 13.6 to 41 eV for deuterium.[37]

Using the plasma density evolution equations (A.14) in (A.16) and (A.21), we find equations of evolution for the ion and electron temperatures:

$$\partial_t T_i = (h_{iz} + h_{cx}) n_0 \left( \frac{2}{3} E_0 - T_i \right) + \dots \quad (\text{A.22})$$

and

$$\partial_t T_e = -h_{iz} n_0 \left( \frac{2}{3} E_{iz} + T_e \right) + \dots \quad (\text{A.23})$$

These are the forms of the ion and electron energy equations solved in the nSOLT model.

The ion momentum equation (A.15) implies a sum of CX and IZ force densities acting on the plasma flow:

$$\mathbf{f} = h_{cx} n_i n_0 (\mathbf{v}_0 - \mathbf{v}_i) + h_{iz} n_e n_0 \mathbf{v}_0. \quad (\text{A.24})$$

In the plane perpendicular to the B-field, the total ion fluid velocity is the sum of the  $E \times B$  and ion diamagnetic drifts,  $\mathbf{v}_i = \mathbf{b} \times \nabla \phi + \mathbf{b} \times \nabla P_i / n_i$ . The evolution of  $n_i \mathbf{v}_i$  follows from charge conservation,  $\nabla \cdot \mathbf{J}_\perp + \nabla_{//} J_{//} = 0$ , including ion gyro-viscous terms, [38] [9] and may be written as an evolution equation for the generalized vorticity,  $\rho \equiv -\nabla \cdot (n_i \nabla_\perp \phi + \nabla_\perp P_i)$ , extended to include the neutral interaction force (A.24) according to the recipe, [12]

$$\frac{d}{dt} \nabla \cdot (n_i \nabla_\perp \phi + \nabla_\perp P_i) = \mathbf{b} \cdot \nabla \times \mathbf{f} + \dots, \quad (\text{A.25})$$

given here in dimensionless Bohm units. The ellipsis (...) denotes the evolution absent neutrals contained in the SOLT model. For example, a term similar to the neutral force density term,  $\mathbf{b} \cdot \nabla \times \mathbf{f}$ , describes the curvature and grad-B polarizing forces that drive the interchange

instability and propel the blobs in the SOLT model. With the unit vector  $\mathbf{b}$  in the z-direction, we have  $\mathbf{b} \cdot \nabla \times \mathbf{f} = \partial_x f_y - \partial_y f_x$ , as written in Eq. 2(d) of Sec. II.

Equations (A.14), (A.22), (A.23) and (A.25) comprise the plasma evolution equations in the nSOLT model, viz., equations 2(a-d) in Sec. II.

### A3. Discussion of momentum and energy conservation

The  $v_x$ -moment of Eq. (A.6) is

$$\partial_t(n_0 v_{0x}) + \partial_x \int dv_x v_x^2 G = -n_0 v_{0x} (h_{cx} \bar{n}_i + h_{iz} \bar{n}_e) \quad (\text{A.26})$$

where the integral of  $v_x F$  vanishes for the Maxwellian  $F$  (A.8), and the neutral fluid momentum density is  $n_0 v_{0x} = \int dv_x v_x G$ . Adding (A.26) to the y-average of the x-component of the ion momentum equation (A.15) yields

$$\partial_t(n_0 v_{0x}) + \partial_t \langle n_i v_{ix} \rangle_y = -h_{cx} n_0 \langle n_i v_{ix} \rangle_y + \dots, \quad (\text{A.27})$$

where here the ellipsis includes the neutral momentum flux in (A.26). Similarly combining (A.11) and (A.15) yields

$$\partial_t(n_0 v_{0y}) + \partial_t \langle n_i v_{iy} \rangle_y = -h_{cx} n_0 \left( \langle n_i v_{iy} \rangle_y - \bar{n}_i \bar{v}_{iy} \right) + \dots \quad (\text{A.28})$$

It follows that, while ionization conserves neutral + ion momentum, charge exchange does so only if  $\langle n_i v_{iy} \rangle_y - \bar{n}_i \bar{v}_{iy} = 0$  and  $\langle n_i v_{ix} \rangle_y = 0$ , which are trivially true of the 1D plasma evolution ( $\partial_y = 0$ ) described in the main text. These residual momentum terms originate in our use of poloidally averaged plasma densities in the neutral kinetic equation (A.6) and would be absent had we used those mean densities in the plasma equations as well.

The residual momentum terms are the poloidal averages of products of fluctuations,

$$\langle n_i v_{iy} \rangle_y - \bar{n}_i \bar{v}_{iy} = \langle \delta n_i \delta v_{iy} \rangle_y$$

and

$$\langle n_i v_{ix} \rangle_y = \langle n_i v_{Ex} + n_i v_{dix} \rangle_y = - \langle \delta n_i \partial_y \delta \phi + \partial_y P_i \rangle_y = - \langle \delta n_i \partial_y \delta \phi \rangle_y,$$

and are expected to be small in comparison to the mean momentum in the edge region. In the SOL, where fluctuation levels can be large compared to the mean momentum, end-loss along open field lines is also a sink for radial momentum, and it will dominate the residual loss terms if  $n_0 h_{\text{CX}} < 1/\tau_{//}$ , i.e., if CX is slower than parallel loss, which is consistent with the long neutral mean-free-path limit in which the averaging over blob structures is appropriate.

The  $v_x^2$ -moment of (A.6) is

$$\partial_t(n_0 E_0) + \frac{\alpha^2}{2} \partial_x \int dv_x v_x^3 G = h_{\text{CX}} \left[ \frac{\alpha^2}{2} \bar{n}_i \bar{T}_i n_0 - n_0 E_0 \bar{n}_i \right] - h_{\text{iz}} \bar{n}_e n_0 E_0 \quad (\text{A.29})$$

with  $n_0 E_0$  defined in (A.20). Adding (A.29) to the y-average of the ion energy equation (A.16) yields

$$\partial_t(n_0 E_0) + \partial_t \frac{3}{2} \langle n_i T_i \rangle_y = -h_{\text{CX}} n_0 \left( \frac{3}{2} \langle n_i T_i \rangle_y - \frac{\alpha^2}{2} \bar{n}_i \bar{T}_i \right) + \dots, \quad (\text{A.30})$$

where the ellipsis (...) includes the energy flux in (A.29). Ion + neutral energy is conserved

only if  $\frac{3}{2} \langle n_i T_i \rangle_y - \frac{\alpha^2}{2} \bar{n}_i \bar{T}_i = 0$ , as is the case for the 1D plasma evolution described in the main text where, in addition,  $\alpha^2 = 3$  (isotropy) was assumed. Otherwise, (A.30) suggests that CX between isotropic ions and anisotropic neutrals ( $\alpha^2 < 3$ ) is dissipative; for  $\alpha^2 < 3$ , fast ions charge-exchange into fast neutrals whose energy in  $v_y$  and  $v_z$  is (partially, depending on  $\alpha^2$ ) lost to the model. But in the long mean-free-path limit, this CX loss can be insignificant compared to the rate at which neutral energy is lost to the wall. Integrating (A.29) from the edge to the wall, the energy flux term (second on the left) may be approximated as  $(\alpha^2/2) n_0 v_0 E_0$  and the first CX term on the right as  $(\alpha^2/2) h_{\text{CX}} n_0 \bar{n}_i \bar{T}_i \Delta$ , where  $v_0$  is a typical neutral velocity and  $\Delta$  is the distance from the edge to the wall. The ratio of the flux to the CX term is thus  $v_0 E_0 / (v_{0,\text{CX}} \bar{T}_i \Delta) = (\lambda_{0,\text{CX}} / \Delta) E_0 / \bar{T}_i$ , where  $v_{0,\text{CX}} = h_{\text{CX}} \bar{n}_i$  is the neutral CX rate, and  $\lambda_{0,\text{CX}} = v_0 / v_{0,\text{CX}}$  is the mean-free-path. Thus in the long MFP limit the neutral energy flux to the wall dominates the dissipation due to CX.

#### A4. A note on the neglect of radiative recombination

Radiative recombination is potentially a sink for ions and a source for neutrals which we ignore in the modeling. The radiative recombination rate per particle for electron capture to the ground state of hydrogen is

$$h_{\text{rec}} = 5.2 \times 10^{-20} \left( \frac{I}{T_e} \right)^{1/2} \left[ 0.43 + \frac{1}{2} \ln(I/T_e) + 0.469 (I/T_e)^{-1/3} \right] \text{ m}^3 / \text{sec}, \quad (\text{A.31})$$

where  $T_e$  is expressed in electron volts (eV), and the ionization potential energy is  $I = 13.56$  eV. The expression (A.31) is given for  $T_e < 400$  eV in reference [39]. Comparing this rate to that for ionization used in this study, Eq. (8), we find that  $h_{\text{rec}} = h_{\text{iz}}$  at  $T_e = 1.32$  eV, well below the ionization energy, with  $h_{\text{iz}} > h_{\text{rec}}$  if  $T_e > 1.32$  eV. (At  $T_e = I = 13.56$  eV we find  $h_{\text{iz}} = 9.54 \times 10^{-15}$  m<sup>3</sup>/sec and  $h_{\text{rec}} = 4.67 \times 10^{-20}$  m<sup>3</sup>/sec.) Although  $T_e \sim 1$  eV may exist in the immediate neighborhood of the divertor, such low temperatures are not found in our simulations of the edge and SOL for parameters pertinent to NSTX. Recombination would be important if the nSOLT model were adapted for application to the divertor region in detached conditions.

#### A5. nSOLT model equations in one dimension

Here we write the model plasma evolution equations that result from Eqs. 2 (a-e) under the assumption that all fields are independent of  $y$ , the bi-directional independent variable, and only depend on the radial variable ( $x$ ) and on time ( $t$ ). These, along with Eqs. 1, are the 1D model equations solved to obtain the results presented in Sec. IV of the main text.

The 1D model plasma equations are obtained from equations 2 (a-e) by setting all partial  $y$ -derivatives equal to zero,  $\partial_y = 0$ . Under this assumption of no  $y$ -dependence, the convective derivative of each 1D field is zero (e.g.,  $v_E \cdot \nabla n = -\partial_y \phi \partial_x n + \partial_x \phi \partial_y n = 0$ ), and the total time derivative reduces to the partial time derivative ( $d_t = \partial_t$ ). The gradient operator acts only in the  $x$ -dimension,  $\nabla = e_x \partial_x$ . Thus there is only diffusive, but no *turbulent*, radial transport in the 1D model. Notice that all of the terms following  $\nabla_{//} j_{//}$  in Eq. 2 (d) vanish because the velocities  $v_E$  and  $v_{\text{di}}$  are strictly in the  $y$ -direction, viz.,  $v_E = \hat{b} \times \nabla \phi = e_y \partial_x \phi$  and  $nv_{\text{di}} = \hat{b} \times \nabla P_i = e_y \partial_x P_i$ , so that both operators  $v_E \cdot \nabla = \partial_x \phi \partial_y$  and  $nv_{\text{di}} \cdot \nabla = \partial_x P_i \partial_y$  give zero when applied to fields that are independent of  $y$ . Similarly, the curvature drive in Eq. 2 (d),  $-2b \times \kappa \cdot \nabla (P_e + P_i)$ , is absent in 1D. The following equations A.(32-36) constitute the 1D nSOLT plasma model corresponding to Eqs. 2 (a-e) given in Sec. II of the main text.

$$\partial_t n_e = \partial_x (D_n \partial_x n_e) + S_n + h_{\text{iz}} n_0 n_e - \nabla_{//} \Gamma_{//}, \quad (\text{A.32})$$

$$\begin{aligned} \partial_t T_e = & \partial_x (D_{P_e} n_e \partial_x T_e) / n_e - T_e \partial_x (D_n \partial_x n_e) / n_e + (S_{P_e} - T_e S_n) / n_e + \\ & - h_{\text{iz}} n_0 \left( \frac{2}{3} E_{\text{iz}} + T_e \right) - \frac{2}{3 n_e} \nabla_{//} q_{e//} + \frac{T_e}{n_e} \nabla_{//} \Gamma_{//}, \end{aligned} \quad (\text{A.33})$$

$$\begin{aligned} \partial_t T_i = & \partial_x (D_{P_i} n_i \partial_x T_i) / n_i - T_i \partial_x (D_n \partial_x n_i) / n_i + (S_{P_i} - T_i S_n) / n_i + \\ & + (h_{\text{iz}} + h_{\text{cx}}) n_0 \left( \frac{2}{3} E_0 - T_i \right) - \frac{2}{3 n_i} \nabla_{//} q_{i//} + \frac{T_i}{n_i} \nabla_{//} \Gamma_{//}, \end{aligned} \quad (\text{A.34})$$

$$\partial_t \rho = \partial_x^2 (D_\rho \rho) - \partial_x f_y - \nabla_{//} j_{//}, \quad (\text{A.35})$$

with

$$\rho = -\partial_x (n \partial_x \phi + \partial_x P_i). \quad (\text{A.36})$$

Expressions for the parallel gradient terms ( $\nabla_{//} \Gamma_{//}$ ,  $\nabla_{//} q_{e//}$ ,  $\nabla_{//} q_{i//}$ , and  $\nabla_{//} j_{//}$ ) are unchanged from Eqs. 2 (a-d) and are given in our published work. [27]

## References

- 1 C. S. Chang and S. Ku, "Spontaneous rotation sources in a quiescent tokamak edge plasma," *Phys. Plasmas* **15**, 062510 (2008).
- 2 D.P. Stotler, J. Lang, C.S. Chang, R.M. Churchill and S. Ku, "Neutral recycling effects on ITG turbulence," *Nucl. Fusion* **57**, 086028 (2017).
- 3 S.I. Braginskii, "Transport processes in a plasma," *Rev. Plasma Phys.* **1** 205 (1965).
- 4 X. Q. Xu, R. H. Cohen, T. D. Rognlien, and J. R. Myra, "Low-to-high confinement transition simulations in divertor geometry," *Phys. Plasmas* **7**, 1951 (2000).
- 5 C. Wersal and P. Ricci, "A first-principles self-consistent model of plasma turbulence and kinetic neutral dynamics in the tokamak scrape-off layer," *Nucl. Fusion* **55**, 123014 (2015).
- 6 B. Zhu, M. Francisquez and B.N. Rogers, "Global 3D two-fluid simulations of the tokamak edge region: Turbulence, transport, profile evolution, and spontaneous  $E \times B$  rotation," *Phys. Plasmas* **24**, 055903 (2017).
- 7 B. D. Dudson and J. Leddy, "Hermes: global plasma edge fluid turbulence simulations," *Plasma Phys. Control. Fusion* **59**, 054010 (2017).
- 8 J. Madsen, V. Naulin, A.H. Nielsen and J. Juul Rasmussen, "Collisional transport across the magnetic field in drift-fluid models," *Phys. Plasmas* **23**, 032306 (2016).
- 9 D. A. Russell, D. A. D'Ippolito, J. R. Myra, J. M. Canik, T. K. Gray, and S. J. Zweben, "Modeling the effect of lithium-induced pedestal profiles on scrape-off-layer turbulence and the heat flux width," *Phys. Plasmas* **22**, 092311 (2015).
- 10 D. Galassi, P. Tamain, H. Bufferand, G. Ciraolo, Ph. Ghendrih, C. Baudoin, C. Colin, N. Fedorczak, N. Nace and E. Serre, "Drive of parallel flows by turbulence and large-scale  $E \times B$  transverse transport in divertor geometry," *Nucl. Fusion* **57**, 036029 (2017).
- 11 The Boussinesq approximation is the neglect of the density gradient in the definition of the generalized vorticity, Eq. (2e).
- 12 S. I. Krasheninnikov, D. A. D'Ippolito and J. R. Myra, "Recent theoretical progress in understanding coherent structures in edge and SOL turbulence," *J. Plasma Phys.* **74**, 679 (2008).
- 13 D. A. D'Ippolito, J. R. Myra and S. J. Zweben, "Convective transport by intermittent blob-filaments: comparison of theory and experiment," *Phys. Plasmas* **18**, 060501 (2011).
- 14 T. D. Rognlien, D. D. Ryutov, N. Mattor and G. D. Porter, "Two-dimensional electric fields and drifts near the magnetic separatrix in divertor tokamaks," *Phys. Plasmas* **6**, 1851 (1999).

- 
- 15 V. Chankin, E. Delabie, G. Corrigan, D. Harting, C. F. Maggi, H. Meyer and JET Contributors, “EDGE2D-EIRENE modelling of near SOL Er: possible impact on the H-mode power threshold,” *Plasma Phys. Control. Fusion* **59**, 045012 (2017).
- 16 D.P. Stotler, C.F.F. Karney, M.E. Rensink and T.D. Rognlien, “Coupling of Parallelized DEGAS 2 and UEDGE Codes,” *Contrib. Plasma Phys.* **40** 221 (2000).
- 17 R. Schneider, X. Bonnin, K. Borrass, D. P. Coster, H. Kastelewicz, D. Reiter, V. A. Rozhansky, and B. J. Braams, “Plasma Edge Physics with B2-Eirene,” *Contrib. Plasma Phys.* **46**, 3 (2006).
- 18 S. Wiesen, D. Reiter, V. Kotov, M. Baelmans, W. Dekeyser, A. S. Kukushkin, S. W. Lisgo, R. A. Pitts, V. Rozhansky, G. Saibene, I. Veselova and S. Voskoboynikov, “The new SOLPS-ITER code package,” *JNM* **463**, 480 (2015).
- 19 N. Bisai and P. K. Kaw, “Role of neutral gas in scrape-off layer of tokamak plasma in the presence of finite electron temperature and its gradient,” *Phys. Plasmas* **23**, 092509 (2016).
- 20 A. S. Thryssø, M. Løiten, J. Madsen, V. Naulin, A. H. Nielsen, and J. Juul Rasmussen, “Plasma particle sources due to interactions with neutrals in a turbulent scrape-off layer of a toroidally confined plasma,” *Physics of Plasmas* **25**, 032307 (2018).
- 21 N. Bisai and P. K. Kaw, “Influence of hot and cold neutrals on scrape-off layer tokamak plasma turbulence,” *Physics of Plasmas* **25**, 012503 (2018).
- 22 A.S. Thryssø, J. Madsen, V. Naulin, and J. Juul Rasmussen, “Influence of molecular dissociation on blob-induced atom density perturbations,” *Nucl. Fusion* **58** 096005 (2018).
- 23 C. Thomser, V. Bailescu, S. Brezinsek, J. W. Coenen, H. Greuner, T. Hirai, J. Linke, C. P. Lungu, H. Maier, G. Matthews, Ph. Mertens, R. Neu, V. Philipps, V. Riccardo, M. Rubel, C. Ruset, A. Schmidt, I. Uytdenhouten, Jet Efd Contributors, “Plasma facing materials for the JET ITER-like wall,” *Fusion Science and Technology* **62** (1), July/August, 1 (2012).
- 24 P. C. Strangeby, “The plasma boundary of magnetic fusion devices,” Taylor and Francis, New York (2000); R. K. Janev, W. D. Langle, K. Evans, Jr. and D. E. Post, “Elementary processes in hydrogen-helium plasmas,” Springer, Berlin (1987).
- 25 C. Wersal and P. Ricci, “Impact of neutral density fluctuations on gas puff imaging diagnostics,” *Nucl. Fusion* **57**, 116018 (2017).
- 26 D.P. Stotler and C.F.F. Karney, “Neutral gas transport modeling with DEGAS 2,” *Contrib. Plasma Phys.* **34**, 392 (1994).
- 27 J. R. Myra, D. A. Russell, and D. A. D’Ippolito, “Transport of perpendicular edge momentum by drift-interchange turbulence and blobs,” *Phys. Plasmas* **15**, 032304 (2008).
- 28 D. P. Stotler, F. Scotti, R. E. Bell, A. Diallo, B. P. LeBlanc, M. Podestà, A. L. Roquemore, and P. W. Ross, “Midplane neutral density profiles in the National Spherical Torus Experiment,” *Phys. Plasmas* **22**, 082506 (2015).
- 29 <http://arks.princeton.edu/ark:/88435/dsp01zg64tp300>
- 30 S. J. Zweben, W. M. Davis, S. M. Kaye, J. R. Myra, R. E. Bell, B. P. LeBlanc, R. J. Maqueda, T. Munsat, S. A. Sabbagh, Y. Sechrest, D. P. Stotler and the NSTX Team, “Edge and SOL turbulence and blob variations over a large database in NSTX,” *Nucl. Fusion* **55**, 093035 (2015).
- 31 In the SOL, the sheath current term in Eq. 2 (d) is  $\nabla_{//} j_{//} = (1 - \exp[(\phi_B - \phi) / T_e]) 2\rho_s / L_{//}(x)$ , where the Bohm potential is  $\phi_B = 3T_e$ , and the parallel connection length,  $L_{//}(x)$ , is the distance measured along the magnetic field line connecting the point at  $x$ , in the outboard midplane, to the divertor sheath.  $L_{//}(x)$  decreases with increasing radius in the SOL because

---

of X-point geometry and the presence of limiters in the far SOL. See ref. [27] for further details.

- 32 G. R. Tynan, I. Cziegler, P. H. Diamond, M. Malkov, A. Hubbard, J. W. Hughes, J. L. Terry and J. H. Irby, "Recent progress towards a physics-based understanding of the H-mode transition," *Plasma Phys. Control. Fusion* **58**, 044003 (2016).
- 33 J. R. Myra, D. A. D'Ippolito, D. A. Russell, M. V. Umansky and D. A. Baver, "Analytical and numerical study of the transverse Kelvin-Helmholtz instability in tokamak edge plasmas," *J. Plasma Phys.* **82**, 905820210 (2016).
- 34 K. H. Burrell, "Effects of ExB velocity shear and magnetic shear on turbulence and transport in magnetic confinement devices," *Phys. Plasmas* **4**, 1499 (1997).
- 35 R. D. Hazeltine, M. D. Calvin, P. M. Valanju and E. R. Solano, "Analytical calculation of neutral transport and its effect on ions," *Nucl. Fusion* **32** (1), 3 (1992).
- 36 G.E. Vekshtein and D.D. Ryutov, "The recombination mechanism of thermal conductivity of a plasma in a strong magnetic field," *Sov. Phys. JETP* **41**, 645 (1976).
- 37 P. C. Strangeby and G. M. McCracken, "Plasma boundary phenomena in tokamaks," *Nucl. Fusion* **30**, 1225 (1990); R. K. Janev, D.E. Post, W. D. Langer, K. Evans, D. B. Heifetz and J. C. Weishei, "Survey of atomic processes in edge plasmas," *J. Nucl. Mater* **121**, 10 (1984).
- 38 A.N. Simakov and P.J. Catto, "Drift-ordered fluid equations for field-aligned modes in low-collisional plasma with equilibrium pressure pedestals," *Phys. Plasmas* **10**, 4744 (2003), and erratum: *Phys. Plasmas* **11**, 2326 (2004).
- 39 J.D. Huba, "NRL Plasma Formulary," Naval Research Laboratory, Washington, DC (2002), pg. 54, Eq. (13).